Surface & Coatings Technology 531 (2026) 133539

Contents lists available at ScienceDirect

Surface & Coatings Technology

journal homepage: www.elsevier.com/locate/surfcoat

Process parameter influences on 17-4PH martensitic stainless-steel coatings produced by extreme high-speed laser cladding (EHLA)

Bohang Gao [a,*], Stefanie Linnenbrink [b], Norbert Pirch [b], Ulrich Krupp [a]

[a] IEHK Steel Institute, RWTH Aachen University, Intzestraße 1, 52072, Aachen, Germany
[b] Fraunhofer Institute for Laser Technology, Steinbachstraße 15, Aachen, 52074, Germany

ARTICLE INFO

Keywords:
Extreme high-speed laser cladding (EHLA)
17-4 PH stainless-steel
Dilution behavior
Processing and thermodynamical modelling

ABSTRACT

Extreme high-speed laser cladding (EHLA) is a promising route for the efficient fabrication of high-performance surface coatings owing to its low dilution and rapid solidification characteristics. Achieving a fully martensitic microstructure in the as-built state, however, remains challenging for 17-4PH stainless steel because of its high Cr content and relatively low martensite-start (Ms) temperature which narrow the processing window. In this work, 17-4PH coatings were successfully fabricated by EHLA. By optimizing the laser processing parameters, fully martensitic coatings were obtained in the as-built state, exhibiting a dense and defect-free microstructure and sound metallurgical bonding to the substrate. Microstructural characterization revealed two distinct dilution mechanisms, namely diffusion-controlled bonding at the coating-substrate interface and convection-induced Cr dilution within the coating interior, with the latter playing a key role in the corrosion resistance of the coating. In addition, phase transformation kinetics were analyzed using thermal histories derived from process simulations. The results show that thermal cycles with peak temperatures within the austenite stability range critically govern the final phase constitution. These findings provide new insights into EHLA processing of martensitic stainless steel and demonstrate the feasibility of designing high-performance stainless-steel coatings.

1. Introduction

The application of protective coatings provide an effective barrier between the substrate and its operating environment, which is crucial for extending service life and ensuring reliable performance under aggressive conditions [1]. Since its introduction in 2017, Extreme High-Speed Laser Cladding (EHLA) [2] has emerged as an economically attractive and technologically advanced solution to prevent premature substrate degradation [3]. Distinguished by its strong metallurgical bonding and exceptionally high deposition rates—typically reaching 50–500 m/min [2,4]—EHLA has enabled rapid progress in the development of hard, wear-resistant coatings [5,6], corrosion-resistant systems [7,8], and hydrogen-embrittlement-mitigating surfaces [9], as well as various other high-performance functional layers [10,11]. To unlock the full potential of EHLA, coating materials must be judiciously selected according to the targeted service environment, accompanied by a rigorous optimization of processing parameters. Owing to their favorable cost-to-performance ratio, stainless-steels have become widely used in surface protection applications [12,13]. Among them, 17-4PH martensitic stainless-steel has attracted particular attention due to its superior strength and antibacterial characteristics, supporting critical uses in aerospace, medical, and chemical sectors [13]. Furthermore, 17-4PH has proven effective as an EHLA cladding material on both low-alloy steels [14] and 304 stainless-steel substrates [15], demonstrating its versatility for advanced surface engineering.

A considerable number of studies have focused on the microstructural features of as-built specimens [16], austenitizing and tempering strategies together with correlations on mechanical performance [11–14,17–22]. Additional efforts have examined Cu and NbC precipitations associated nanoscale strengthening mechanisms [12,13,18,19], as well as compositional modifications aimed at enhancing phase stability and mechanical response [20–24]. Vunnam et al. [21] demonstrated that minor variations in powder chemistry can lead to markedly different phase constitutions in selective laser melting (SLM). Murr et al. [23] and Moyle et al. [24] have also suggested that the shielding gases (Ar vs. N_2) used during the machining process have direct effects on the as-printed state of 17-4PH. Overall, the diversity of reported conclusions can be traced to two principal factors: (i) the direct influence of alloy chemistry on the stability of equilibrium and metastable phases, and (ii) the strong dependence of cumulative phase

* Corresponding author.
E-mail address: bohang.gao@iehk.rwth-aachen.de (B. Gao).

https://doi.org/10.1016/j.surfcoat.2026.133539
Received 6 February 2026; Received in revised form 16 April 2026; Accepted 29 April 2026
Available online 30 April 2026

transformations on process-specific thermal histories, including cooling rates and cyclic reheating. Another considerable body of research has quantified dilution by analyzing melt-pool cross-sections and has examined its relationship with laser processing parameters [25–28]. Studies in which the cladding material exhibits a melting point lower than or comparable to that of the substrate have similarly reported pronounced dilution effects [28,29]. The dilution ratio is predominantly derived from melt-pool geometry, yet detailed chemical-composition validation is largely absent. Li et al. [30,31] revealed the associated gradients in mechanical performance by providing longitudinal hardness. However, the quantitative influence of laser parameters and powder focus distance (PFD) on dilution at the bonding region, as well as dilution phenomena occurring within the coating itself, remains insufficiently understood.

As mentioned in the studies above, austenitization is necessary in additively manufactured 17-4PH to obtain a fully martensitic microstructure as well as post aging for further enhancement of strength [32,33]. As a result, the concept of directly optimizing the as-built condition and employing it as the final product state has not yet received comparable attention. Furthermore, in material combinations involving two or more constituents, such as coating–substrate systems, post heat treatment inevitably affects the mechanical properties of the substrate [34]. These changes posing limitations for applications that require the substrate to retain its original performance.

In this study, an almost fully martensitic as-built 17-4PH coating was obtained by selecting appropriate processing parameters, exhibiting well-bonded and defect-free produced by EHLA. The influence of laser power and PFD on dilution behavior were systematically analyzed. Furthermore, the phase-transformation mechanisms during process were elucidated by combining process simulations with CALPHAD-based kinetics calculations and comparing the results with experimental observations.

2. Methods

2.1. Fabrication and material

A 4-axis lathe with integrated laser optics from Hornet (Hornet Laser Cladding BV, The Netherland), was used as cladding machine (see Fig. 1(a)). The maximum spindle speed is 775 rpm. The Hornet II operator terminal was equipped with a Fanuc CNC control system. The workpieces were clamped in place using a three-jaw chuck mounted on the tiltable spindle. The powder was transported to the processing site and injected into the melt bath using an Oerlikon Metco Twin 150 powder conveyor and the ILT Coax EHLA powder nozzle with coolers and three powder inlets (Fig. 1(b)). The geometry of the powder gas stream was conical and arranged coaxially with the laser beam. Laser line OTZ-5 optics with a zoom function were used as the beam shaping optics. The optics were connected to a laser line LDF 8000–40 diode laser via an optical fiber. To investigate the optimal laser power, laser beam of 1.4 mm diameter with top hat intensity was employed.

The 17-4PH powder supplied by Oerlikon Corporation AG (OCAG, Switzerland) and was fabricated with gas atomization in Argon atmosphere, the respective chemical composition is shown in Table 1. Powder size distributions with respect to amount and volume after sieving were included in Fig. 2(a) and Fig. 2(b) together with accumulative distribution, respectively. The particle size distribution measurements were performed with Camsizer X2 (Retsch GmbH, Germany). The primary diameter of the powder particles was concentrated between 20 and 60 μm. Round bars fabricated with low-alloy steel S355 J2 + M (composition in Table 1) with a diameter of 50 mm and a length of approx. 400 mm were used as substrates.

2.2. Processing parameter and sample geometry

Four laser power levels, 2500 W, 2750 W, 3000 W, and 3250 W, were selected to fabricate the coatings in order to investigate the influence of laser power on coating performance. This is to achieve adequate coating-substrate bonding and minimize coating defects. In addition to laser power, the powder focus distance (PFD) also influences the dilution behavior at the coating–substrate interface. Therefore, characterization of the powder gas stream is required to assess its effect on material deposition and mixing. The characterization of the powder gas stream was carried out in a plane-wise manner as shown in Fig. 3(a), using a dedicated powder stream analysis system. During the measurements, the powder stream was illuminated by a laser beam-oriented perpendicular to the powder–gas flow direction, while the spacing between measurement planes was reduced in the region of the powder focus. A coaxially aligned high-speed camera operating at approximately 12,000 Hz recorded roughly 10,000 images per plane, with an effective illumination thickness of approximately 0.2 mm.

Table 1
Chemical composition of 17-4PH-D powder and substrate S355 J2 + M in weight percent (wt%).

	Fe	Cr	Ni	Cu	Si	Mn	C	Nb
17-4PH-D	Bal.	17.0	4.5	4.0	1.0	0.6	0.07	0.3
S355 J2 + M	Bal.	0.05	0.07	0.2	0.22	1.09	0.17	0.002

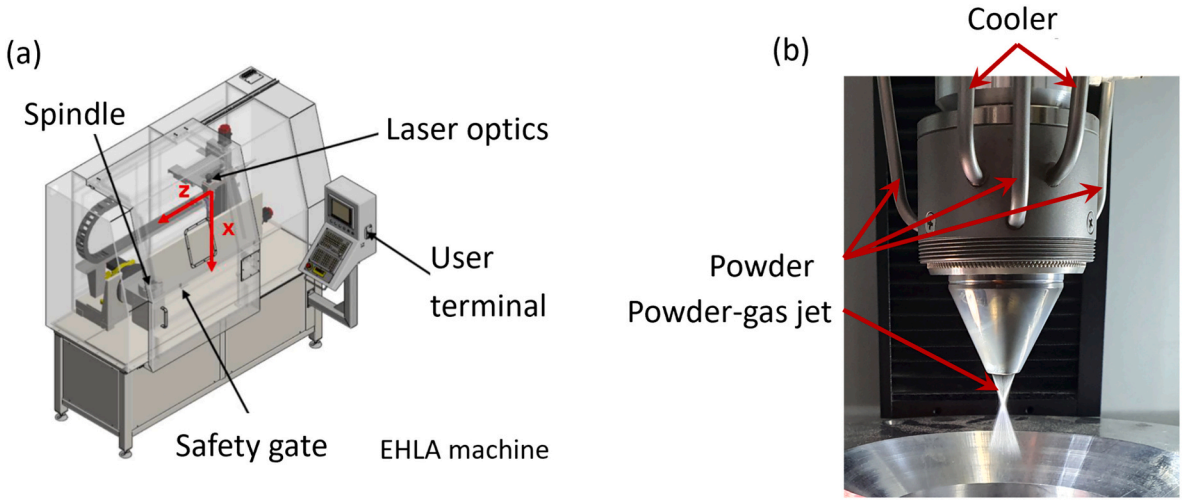

Fig. 1. (a) Sketch of EHLA machine and (b) ILT Coax EHLA powder nozzle.

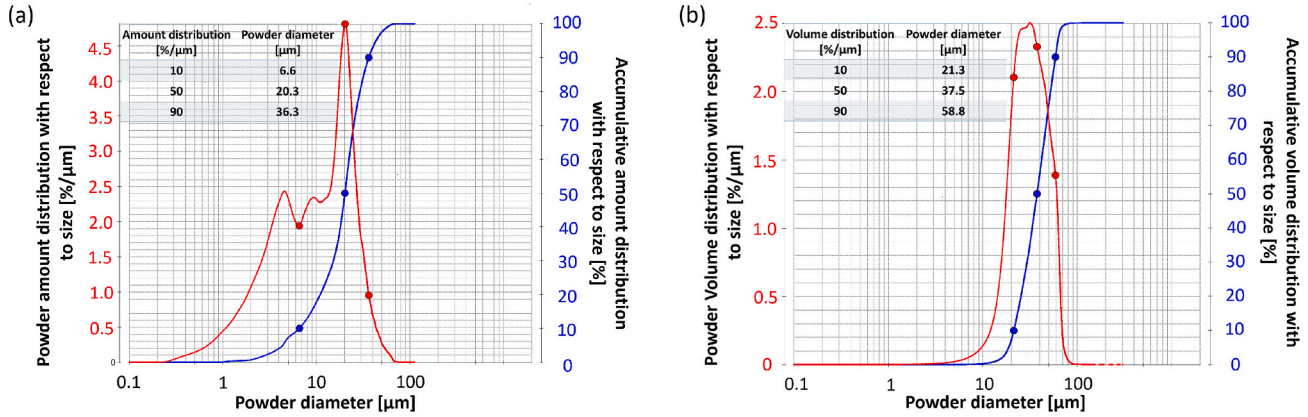

Fig. 2. Powder size distribution with respect to (a) amount fraction and (b) volume fraction. The particle diameters of cumulative distributions of 10%, 50%, and 90% (D10, D50, and D90) are marked at the corresponding positions in respective figures.

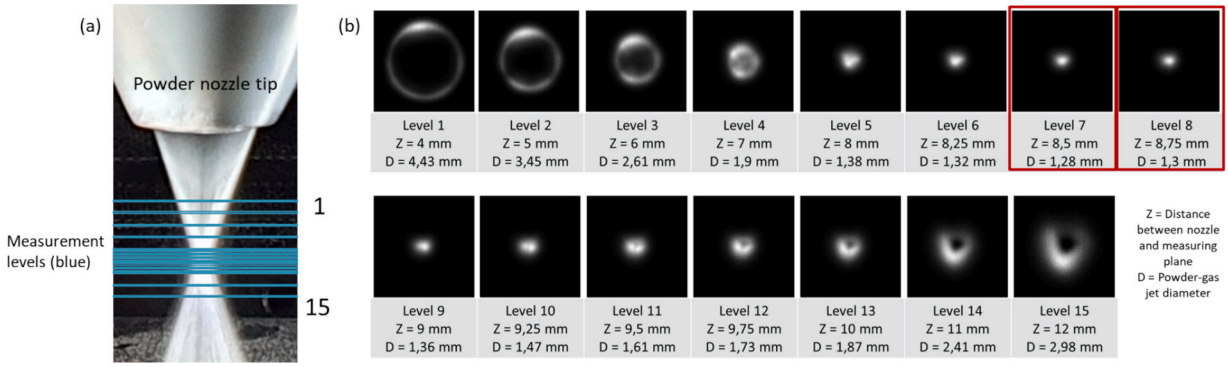

Fig. 3. Powder nozzle tip in (a) with measuring height in blue lines, level 1 to 15 from top to bottom, and measurements of powder focus cross section in (b) with height Z in mm and diameter D in mm accordingly. (For interpretation of the references to colour in this figure legend, the reader is referred to the web version of this article.)

In the vicinity of the nozzle tip, the powder stream cross-section exhibited a ring-shaped structure. With increasing distance from the nozzle, the ring diameter decreased progressively until a point-like cross-section was obtained at the powder focus (Fig. 3(b), Level 6 to Level 9). The measurements further revealed that the powder stream was not fully homogeneous in regions where a ring-shaped cross-section occurred. Instead, localized particle agglomerations were observed, which can be attributed to the configuration of the three powder inlets.

Since the laser spot diameter was measured to be 1.4 mm, the powder convergence diameter should remain within this value, for the following reasons: If the diameter of the laser beam is larger than the powder focus, higher powder efficiency can be expected, and secondly, to prevent the central region of the laser beam from passing through a defocused powder stream and directly irradiating the substrate, which would lead to excessive substrate melting and undesired dilution. Therefore, the PFD between the fifth and ninth levels were of ideal range.

For the experiments, the powder focus setting at level 7 with powder convergence diameter 1.28 mm was used as the reference position. When this focus plane coincided precisely with the substrate surface, the PFD was defined as 0 mm. A positive PFD value corresponds to an upward shift of the powder focus, indicating the distance above the substrate surface. In this study, PFD values of 0 mm, 0.5 mm, and 0.75 mm were selected. Combined with four laser power levels ranging from 2500 W to 3250 W, a total of twelve samples were fabricated. The corresponding processing parameters are listed in Table 2.

A schematic of the sample geometry is shown in Fig. 4(a). The X-axis (spatial coordinate in green) is always parallel to the longitudinal axis direction of the rod-shaped substrate, which is also the build direction. This spatial coordinate system was also used in the subsequent EBSD sample coordinate system. Each deposited track exhibited a nominal coating width of 10 mm, and adjacent coatings were spaced 2 mm apart. To characterize the microstructure and evaluate coating performance, samples were sectioned along both the longitudinal (build) direction and the circumferential (transverse) direction, as illustrated in Fig. 4(b). The spatial coordinate XYZ will be used for all subsequent measurements.

Sample denomination with respect to parameters are shown in

Table 2
EHLA processing parameter set.

Laser beam diameter (mm)	Offset per track (mm)	Build-rate (m/min)	Powder mass flow (g/min)	Carrier gas (Ar) flow (l/min)	Shielding gas (Ar) (l/min)	Laser power (W)	Powder focus distance (PFD) (mm)
1.4	**0.2**	**50**	**26.2**	**6.5**	**10**	**2500** **2750** **3000** **3250**	**0** **0.5** **0.75**

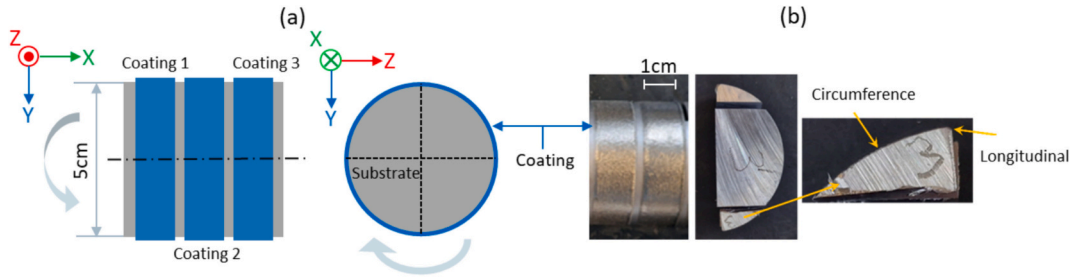

Fig. 4. (a) sketch of sample geometry with spatial coordinate and rotation during processing. (b) actual samples and cutting, spatial coordinates are shared with those in (a).

Table 3
Parameters and denomination of EHLA samples.

Sample No.	Laser power (W)	Powder focus (mm)	Sample No.	Laser power (W)	Powder focus (mm)
1	2500	0	7	3000	0.5
2	2750	0	8	3250	0.5
3	3000	0	9	2500	0.75
4	3250	0	10	2750	0.75
5	2500	0.5	11	3000	0.75
6	2750	0.5	12	3250	0.75

Table 3. PFD represents the spatial height difference between the horizontal plane of powder focus and the substrate surface tangential to this plane.

2.3. Microstructural characterization methods

Optical microscopy Keyence VHX-600 digital microscope (Keyence GmbH, Germany) was used to evaluate coating quality via micro-defect observation and bonding continuity. The samples were ground up with 2500 SiC grid paper, followed by mechanical polishing with 6, 3 and 1 μm diamond suspension. Samples were etched with in V2A-Beize solution (Struers GmbH, Germany) which is a mixed-acid solution based on nitric acid (HNO_3) and hydrofluoric acid (HF)with water and cleaned with ethanol. Etching was carried out at 60 °C with duration of 10s.

Scanning electron microscopy (SEM) energy dispersive X-ray diffraction (EDS), and Electron backscatter diffraction analysis (EBSD) were performed on a Zeiss Sigma field emission gun SEM (Carl Zeiss Microscopy, Oberkochen, Germany) equipped with EBSD and EDS detectors by Oxford Instruments (Abingdon, UK). For EDS, a 20 kV electron beam was used to measure the metallic elements Fe, Cr, Ni, Cu, Mn, and Nb. For EBSD, voltage of 16 kV with a working distance of 15–17 mm was chosen. The step size was selected accordingly based on size of scanning area: a step size of 0.3 μm was used for large area scannings, while a finer step size of 0.1 μm with fixed scanned area of 240 × 200 μm was adopted for slice scans aimed at investigating microstructure. The exact center of all EBSD mappings corresponds to the central region of the selected area, thereby eliminating systematic errors caused by asymmetry in the selection. Analysis and reconstruction of EBSD data were carried out with the MATLAB® (Mathworks, USA) based MTEX toolbox [35].

2.4. Mechanical characterization methods

Hardness testing (Vickers method) was carried out using a ZHμ microhardness tester (Zwick/Roell GmbH & Co. KG, Germany) with diamond pyramid according to ISO 6507 and ASTM E384. 200gf (HV0.2) was selected as defined test load. For each condition, ten indentations were conducted. The maximum and minimum values were excluded, and the mean hardness was determined from the remaining data.

2.5. Processing simulation and CALPHAD modelling

An in-house simulation tool developed by the Fraunhofer ILT was used to calculate the spatially resolved temperature profiles within a track and the subsequent in situ heat treatment caused by the following tracks. This tool uses the finite element method to numerically solve the free boundary value problem for powder-based laser cladding. A recent update to the tool now also addresses the multiple reflections within the powder cloud that are relevant to the EHLA process [36]. The resulting high gradients within the process zone require a resolution of approximately 5 μm for the element edge length in this zone.

Due to the resulting high number of nodes, this cannot be achieved over the entire cylinder. Therefore, only a section of the cylinder containing the process zone and its boundary area was selected for the finite element mesh. For the overlap tracks calculated on this section, a waiting time corresponding to the circulation time on the cylinder was applied for each subsequent track. Since the coating material shares similar physical properties with the substrate, the following parameters are applied to both. Important physical properties and parameters are listed in Table 4.

Track formation on a cylindrical surface has proven to be extremely complex. Therefore, the calculation for layer formation was carried out on a flat surface, as shown in Fig. 5. To reduce modelling complexity resulting from enhancing the powder focus, the process simulation considers a PFD of 0 mm as the starting condition. The preheating calculated on the cylindrical geometry shown in Fig. 5 was used as input into the module for track development. At the end of each track, a waiting time was applied that corresponds to the length of the remaining circulation time on the rod.

Equilibrium phase diagrams were calculated using Thermo-Calc® software [37] (2023b release, Thermo-Calc Software, Sweden) with database TCFE10 v10.1. Matcalc® software (version 6.04) [38] along with the thermodynamic (‘mc_Fe.tdb’, version 2.023) and diffusion (‘mc_Fe.ddb’) databases were employed to simulate the kinetic evolution of matrix phases in 17-4PH alloy system during EHLA processing. The kinetic simulation in MatCalc is based on classical nucleation theory and the Svoboda-Fischer-Fratzl-Kozeschnik (SFFK) growth model [39]. Temperature – time relations were generated from process modelling.

3. Result and discussion

3.1. Coating morphology

To provide a more intuitive presentation of the quality of the EHLA

Table 4
Physical properties and parameters for processing simulation.

Properties and parameters	Material density ρ (kg/mm^3)	Heat capacity $C_p(J/kg/k)$	Energy Absorption rate	Ambient temperature T (K)
	7.8×10^{-6}	500	0.59	298

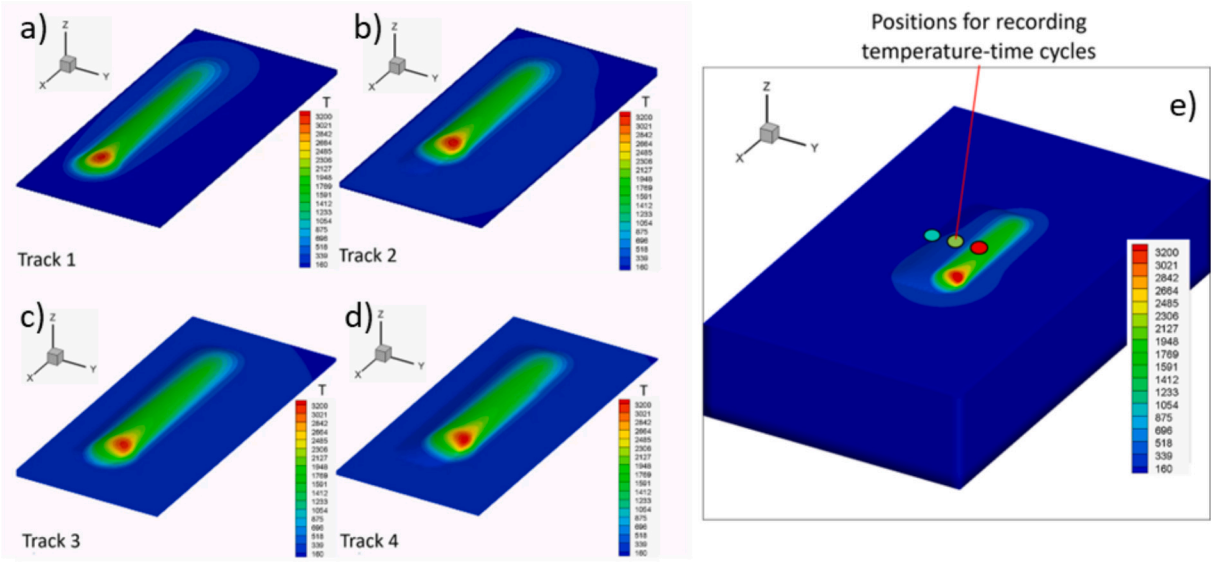

Fig. 5. Temperature development during the process for 4 tracks (left) and (e) positions for recording the temperature-time cycles as an example. The colour bar indicates a temperature range from 100 to 3200 °C.

coatings obtained under different processing conditions, the LOM micrographs of all samples are compiled in Fig. 6. For each sample group, the coatings were examined in both orthogonal cross-sections (the circumferential direction and the longitudinal direction). For each sample, the coating thickness was measured at 10 locations. In the longitudinal direction (Fig. 6a), the maximum and minimum thickness values were indicated separately. Since the laser spot diameter was 1.4 mm and the offset between adjacent tracks was 0.2 mm, the coating length near the beginning and the end of the cladding path contained fewer accumulated tracks than the steady-state region. Therefore, these edge regions were excluded from the thickness evaluation, and the mean coating thickness was determined only from the remaining steady-state region. An example of the steady-state region is marked for the 2500 W, 0 mm sample in the Fig. 6a. The coating thicknesses measured in the circumferential and longitudinal directions for all sample groups are presented in Fig. 7(a) and (b), respectively. It can be seen that under all processing conditions, the mean coating thickness in circumferential directions were approximately 250 μm. In the longitudinal direction, no clear dependence of the mean coating thickness on the processing condition was observed, and the thickness values exhibited a larger scatter than those measured in the circumferential cross-section.

The measurement of the dilution depth and the calculation of the dilution ratio were conducted in a manner similar to that commonly adopted in conventional DED studies [40,41]. The coating thickness, H, was defined as the vertical distance from the original substrate surface to the top surface of the deposited layer, whereas the dilution depth, D, was defined as the penetration depth of the molten zone extending below the original substrate surface. Following the geometrical description commonly used for laser-clad cross-sections, the dilution ratio was calculated according to Eq. (1) [41]:

$$\eta = \frac{D_{mean}}{H + D_{mean}} \times 100\% \quad (1)$$

For each processing condition, 10 values of D were measured, and the average value, D_{mean}, was used to calculate the dilution ratio. The results are shown in Fig. 7(c).

In addition to the average dilution depth, the maximum dilution depth, D_{max}, was measured, as shown in Fig. 7(d). To quantify the stability of the dilution depth, a dilution-depth ratio, a, was defined as shown in Eq.2.

$$\alpha = \frac{D_{mean}}{D_{max}} \times 100\% \quad (2)$$

The results for the dilution-depth ratio are presented in Fig. 7(e). If the melt pool exhibits a regular period corresponding to the track offset and the dilution depth remains constant, then a approaches 100% (Fig. 7 (f) upper).

For the same PFD, increasing the laser power clearly increased the dilution depth, thereby further increasing the dilution ratio. At a constant laser power with three different PFD values, both the average dilution depth and the maximum dilution depth showed a slight increase, except for the lowest laser power of 2500 W. For the coatings produced with 2500 W, the average dilution depth remained nearly unchanged across different PFD values, and a similar trend was observed for the maximum dilution depth. Compared to the samples processed with less PFD, the samples processed at a PFD of 0.75 mm exhibited the highest dilution-depth ratio. In addition, increasing the laser power also led to an increase in the dilution-depth ratio. This indicates that, within a certain range, increasing the PFD can result in a more stable dilution depth, as schematically illustrated in Fig. 7 (f). On the other hand, within the PFD range of 0–0.75 mm, the effect of PFD on the dilution depth can be considered negligible, and the dilution depth was mainly governed by the laser power, increasing with increasing laser power. Combined with the weak correlation between the coating thickness and both PFD and laser power, the coating morphology suggests two possible directions for process optimization:(1) reducing the laser power to decrease the dilution ratio; and (2) increasing the PFD to obtain a more homogeneous dilution depth. Other effects of laser power on the dilution behavior will be further discussed in Section 3.5.

3.2. Hardness measurement

Representative hardness profiles of the coatings were obtained and compared across all samples as shown in Fig. 8. Particular attention was paid to the region near the coating–substrate interface. The hardness on the coating-adjacent sides of the interfaces exhibited the same variation trend as that of the coating and were slightly higher in all cases. The maximum hardness is observed in the No. 4 (3250 W, PFD = 0 mm) up to 392$HV_{0.2}$.

Since the final coating undergoes a turning operation, the in-service coating thickness is smaller than the as-built thickness; therefore, the hardness test was selected to be performed at a distance of 150–200 μm

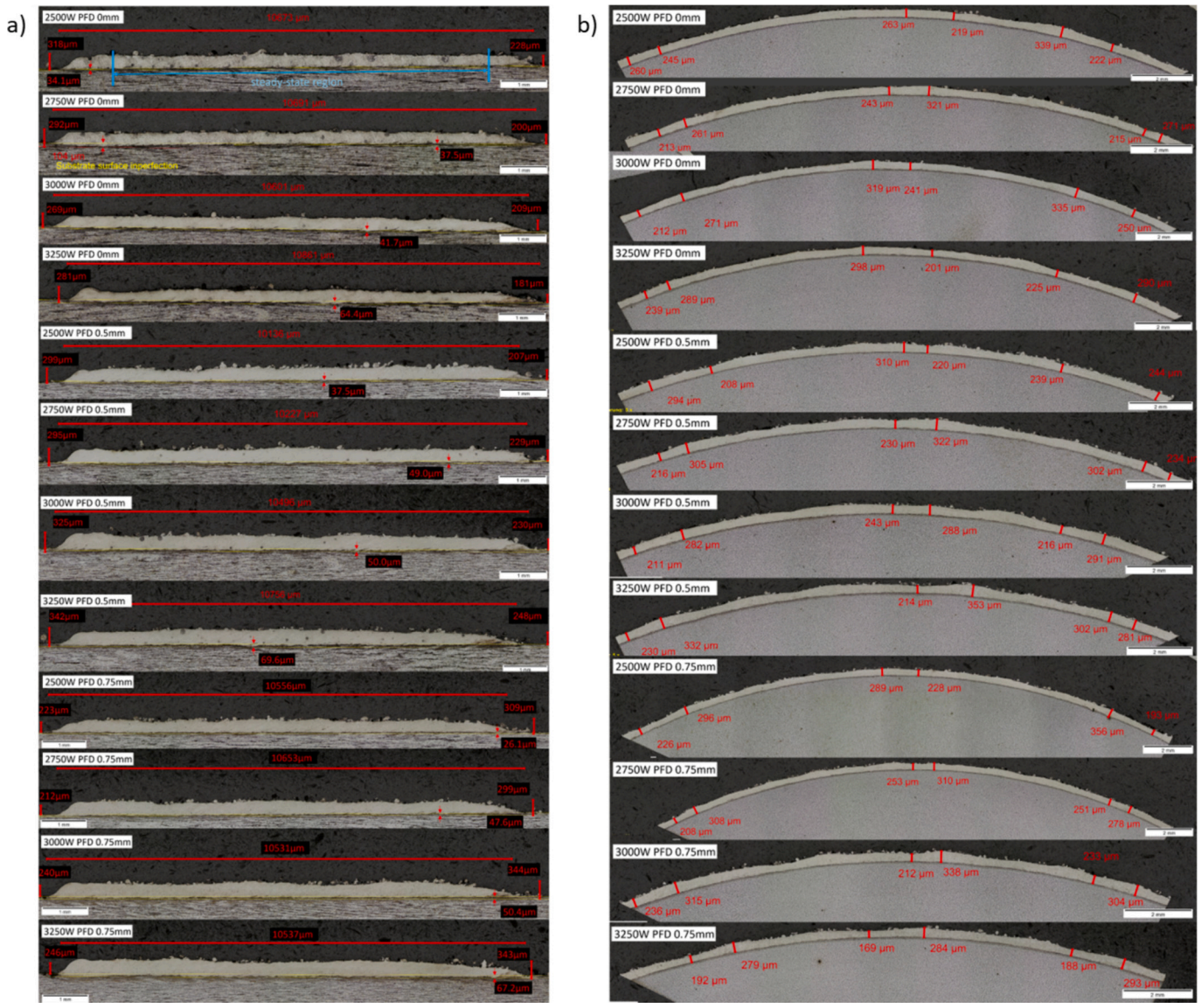

Fig. 6. LOM images of all coatings: (a) along longitudinal direction and (b) circumferential cross-section direction.

from the coating-substrate interface, denominated coating top. For samples processed with the same powder focus height, the microhardness increased with increasing laser power. At a fixed laser power, a slight decrease in hardness was observed as the PFD was increased. In the case of the coatings with powder focus distance at 0.75 mm, the hardness exhibited only a marginal increase when the laser power was raised from 2750 W to 3250 W. Among all as-built samples, Sample No.4 (3250 W, PFD = 0 mm) showed the highest average hardness, reaching 392 HV0.2. Based on these observations, Samples No.1–4 (PFD = 0 mm) were selected to investigate the influence of laser power on the microstructure, dilution, and phase evolution, whereas samples No.4, No.8 and No.12 (3250 W) were used to examine the effect of the powder focus parameter.

3.3. *Influence of laser power on the coating microstructure*

Since laser power significantly affects coating hardness, to investigate its influence on microstructure, samples No. 1 and No. 4—representing the lowest and highest laser powers—were first selected for comparison. During the EHLA procedure, the process follows a repetitive sequence: after each full rotation of the substrate, the subsequent track is deposited on top of the previously solidified material. If the process terminates at this stage, the most recently deposited track forms the terminal edge of the coating. By extension, the thermal cycles and phase-transformation history experienced by any individual track over time can be considered equivalent to the cumulative thermal and transformation history imposed on several preceding, adjacent tracks during the deposition of the current track. Consequently, the terminal region of the coating was selected for analyzing microstructural evolution. In analogy to previous welding and AM studies that exploit spatially resolved characterization along the build or weld direction as a proxy for in-situ phase transformation analysis [42–44], the present work investigates different positions within the same EHLA coating to reconstruct the cumulative thermal and phase-transformation history.

Fig. 9 (a) and (b) show the etched cross-section of the coating taken along the longitudinal (axial) direction of sample No.1 (2500 W PFD = 0 mm) and No.4 (3250 W PFD = 0 mm) with LOM. The spatial reference frame is defined as follows: the *Z*-axis points outward, perpendicular to the observation plane, while X and Y correspond to the horizontal and vertical directions of the sample, respectively. Metallurgical bonding was observed between the coating and the substrate, and no internal defects are detected within the coating. The coating exhibits a uniform thickness of approximately 250 μm above substrate surface.

A clear contrast can be observed between the different laser power

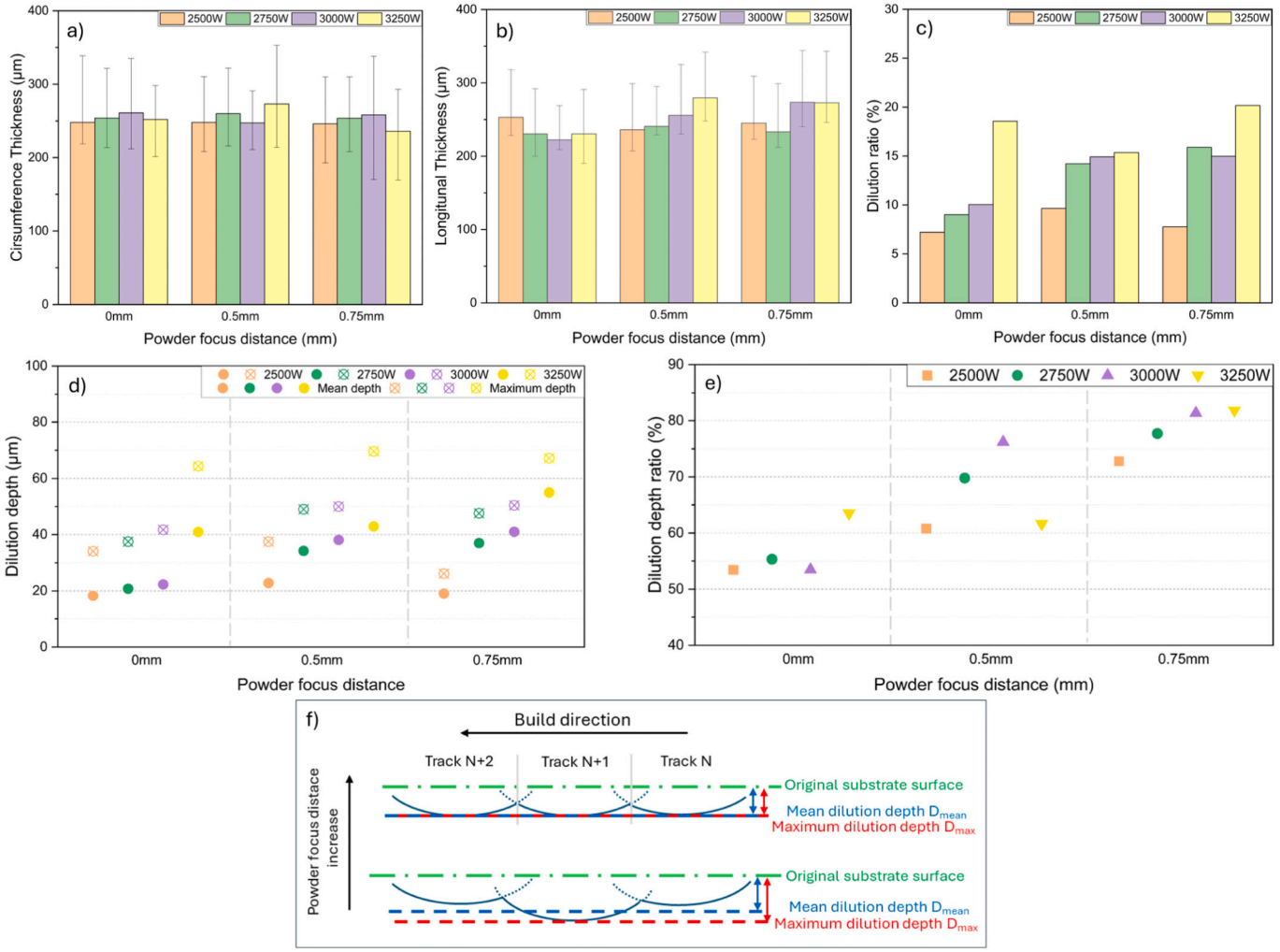

Fig. 7. (a) and (b) represent the coating thickness in the circumferential and the longitudinal cross-sections, respectively. (c) Dilution ratio results, (d) mean and maximum dilution depth results (e) dilution depth ratio; and (f) schematic diagram show showing dilution depth and related parameters. The upper figure illustrates ideal, stable cladding, where each track exhibits the same dilution depth, while the lower figure depicts the non-uniform dilution depth observed in actual processes; this phenomenon is particularly pronounced in the 0 mm PFD.

levels: at 2500 W, the layer boundaries within the coating remain relatively straight, whereas at 3250 W these boundaries become noticeably more curved and complex. This behavior is consistent with observations reported in DED studies [25,45,46], where the melt-pool penetration depth increases with increasing laser power. In addition, a significant population of elongated columnar grains was observed near the top region of the 2500 W coating. These grains correspond to soft ferritic structures, with maximum observable lengths of approximately 100 μm. In contrast, the 3250 W coating exhibited only a small fraction of short columnar grains confined to the coating top. Because these surface grains will be remelted during the subsequent turning operation, the unmelted parts will remain inside the coatings.

During deposition, the substrate completes one full rotation while the laser advances by 0.2 mm in the negative X-direction, resulting in a theoretical inter-track spacing of 0.2 mm. This spacing is indicated by the blue arrows in both samples in Fig. 9 which represent the center-to-center distance between adjacent layers. Considering a laser spot diameter of 1.4 mm, the spot spans roughly seven such spacing intervals. The etched melt-pool boundaries (highlighted by red curves) represent the actual layer boundaries, and their spacing is indicated by the yellow arrows. Additionally, less pronounced melt-pool boundaries are also visible (orange dash lines). It is evident that the actual inter-layer spacing does not always coincide with the theoretical spacing; only a portion of the layers align with the predicted positions (marked by green boxes). This is related to the stability of powder carrier gas flow during high-speed rotation. Furthermore, due to the convex surface formed after solidification of the molten pool, the subsequent track produces an asymmetric, S-shaped melt boundary. As a result, the normal direction of the melt line forms a noticeable inclination around 30° relative to the X-axis.

To more accurately resolve the microstructural features—particularly the phase constitution—EBSD measurements were performed in the LOM-identified regions, and the resulting EBSD-IPF maps were overlaid with the corresponding LOM images, as shown in Fig. 10. The EBSD colour key was oriented such that the [001] crystallographic orientation is parallel to the sample *Z*-direction (out of plane). The high-contrast red layer boundary identified in the LOM image was retained and superimposed above the EBSD map for direct comparison.

The EBSD scan area was selected based on the following considerations. Firstly, the thermal input within the laser spot directly affects the coating over an equivalent surface area; therefore, the scan width was set to match the laser diameter of 1.4 mm. Secondly, the region corresponds to the hardness measurement locations and is representative of the final coating thickness. To avoid the influences near the coating–substrate interface, the EBSD scan height was limited to 200 μm.

By comparing samples processed with the same powder focus but

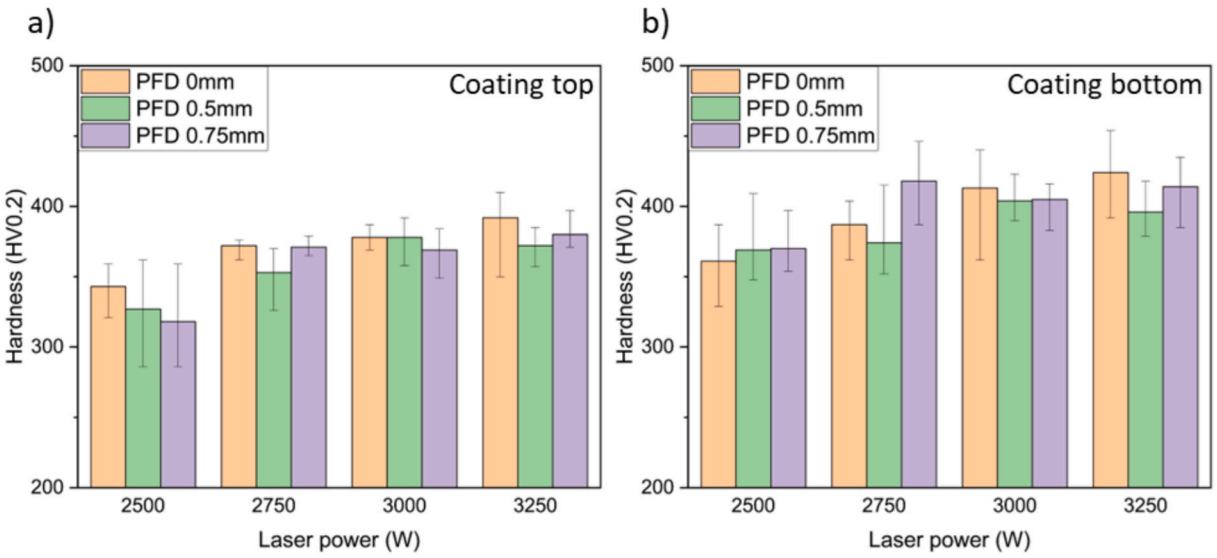

Fig. 8. Coating hardness results: (a) coating top and (b) coating bottom near the coating-substrate interface (HV0.2). For each sample, ten hardness values were measured; the maximum and minimum values were excluded, and the remaining values were averaged to obtain the mean hardness. Hardness measurement errors are also shown.

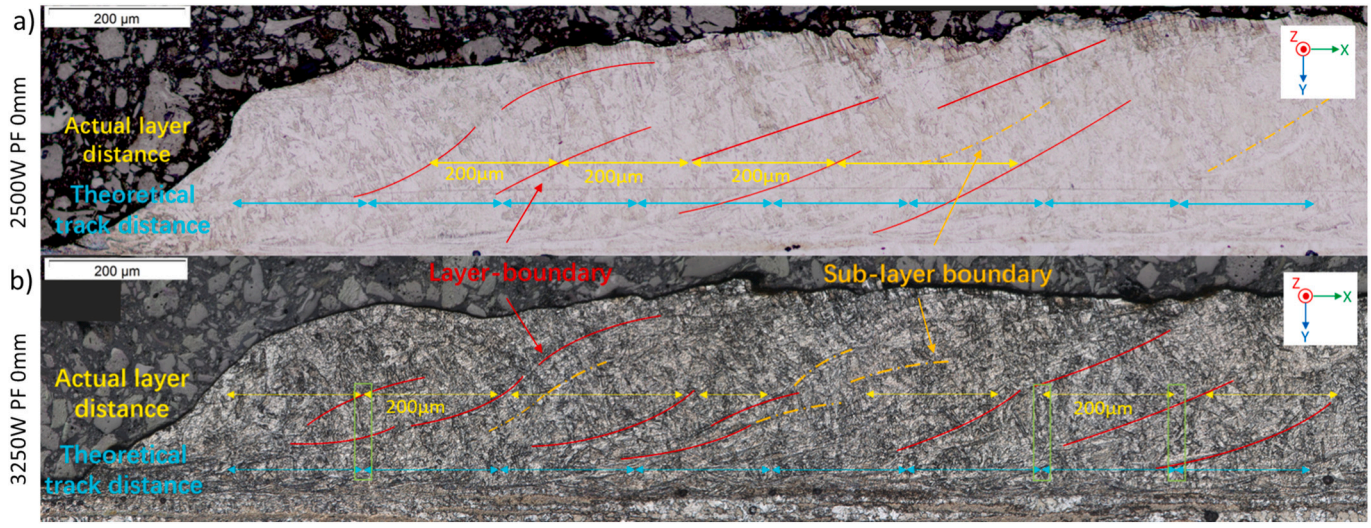

Fig. 9. LOM result of etched No.1 (2500 W PFD0mm) and No.4 (3250 W PFD0mm) samples. The blue arrow indicates the theoretical track distance, while the yellow arrow represents the actual track spacing. The red and orange lines denote the layer boundary (fusion line). (For interpretation of the references to colour in this figure legend, the reader is referred to the web version of this article.)

different laser energy inputs, clear differences in microstructural morphology can be observed. The coating of Sample No. 4 (3250 W, PFD = 0 mm) exhibits an almost fully martensitic structure across the entire analysis area, and the long axes of the grains show a more pronounced inclination toward the build-direction (negative X-direction) compared with those in Sample No. 1 (2500 W, PFD = 0 mm). This behavior is associated with the geometry of the layer boundary. As demonstrated earlier in the LOM results, a higher laser power produces a more strongly curved layer boundary, and the solidification thermal gradient generally aligns with the local normal to this boundary. Consequently, the grain long axes orient at a larger angle relative to the surface normal. In Sample No. 1 (2500 W, PFD = 0 mm), elongated columnar ferrite grains originating from the melt pool of previous layer extend into the mid-thickness of the coating, resulting in a mixed microstructure of martensite with a small amount of columnar ferrite. This explains the lower hardness observed in this coating.

3.4. Influence of laser power on phase evolution

Using the TCFE10 thermodynamic database in Thermo-Calc, the equilibrium phase diagram of 17-4PH stainless steel was calculated, as shown in Fig. 11(a). The thermodynamically stable phases are indicated, comprising of the liquid phase at high temperatures (above 1447 °C), the austenite domain region at intermediate temperatures (767 °C–1314 °C), and the ferrite region at lower temperatures (below 767 °C). Fig. 11(b) presents a representative temperature–time profile at the substrate surface for a single-track during processing. The temperature axis is aligned with that of the equilibrium phase diagram, and the potential matrix phases during the heating and cooling cycle of the track are annotated based on the relationship between equilibrium and metastable phase formation.

Thermo-Calc predicts an Ac_1 temperature of approximately 740 °C and an Ms. temperature of approximately 139 °C. From the thermal history, the cooling path between Ac_1 and Ms. exhibits sufficiently high,

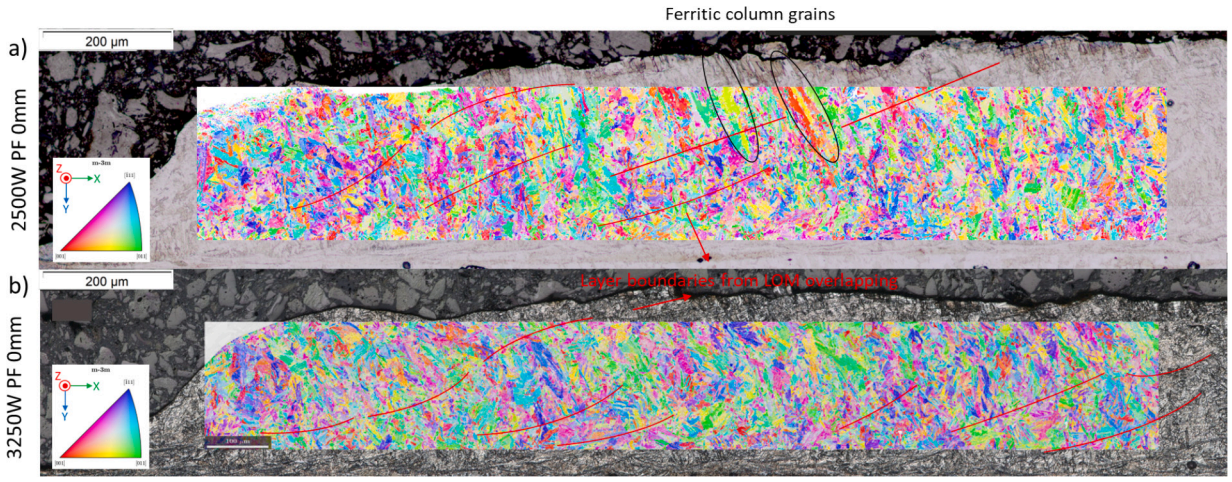

Fig. 10. The EBSD mapping overlaid with the LOM image, with the layer boundary retained in red for No.1 (2500 W PFD0mm) and No.4 (3250 W PFD0mm) samples. The columnar grains of sample No.1 highlighted with black circles in (a). (For interpretation of the references to colour in this figure legend, the reader is referred to the web version of this article.)

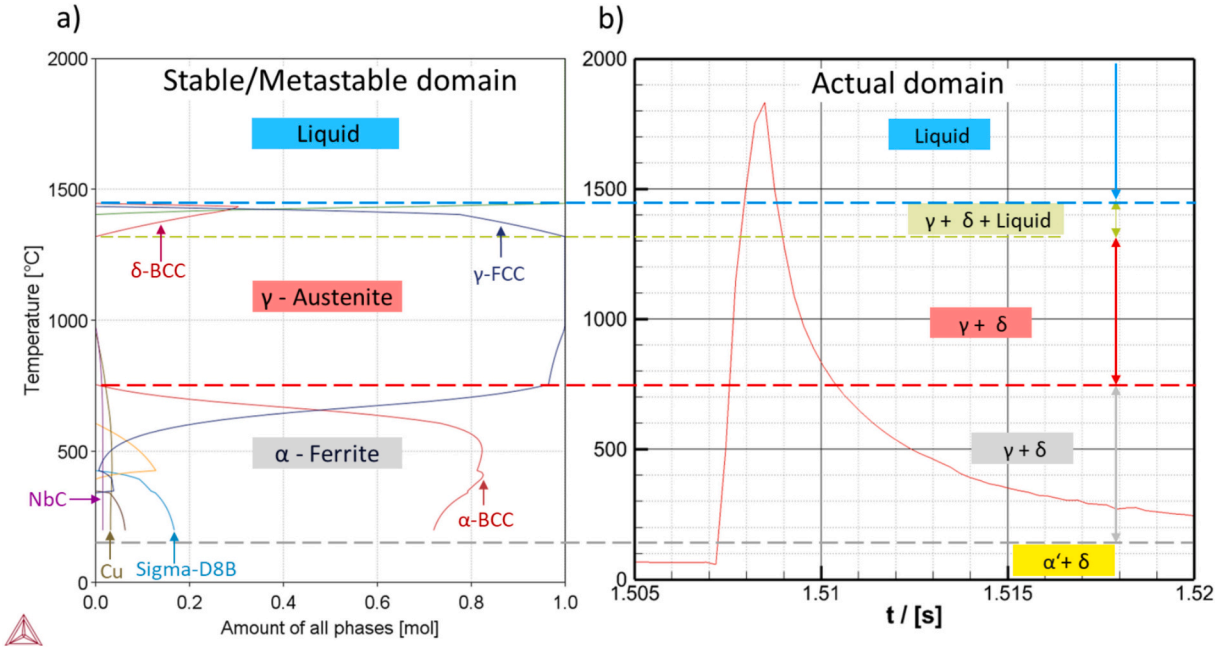

Fig. 11. (a) Equilibrium phase of 17-4PH with stable or metastable domain and, (b) sketch of temperature history in one track. The vertical axis represents the aligned temperature.

thereby suppressing ferrite formation and promoting the transformation of undercooled austenite into martensite.

Based on the temperature-phase equilibrium relationships established during the aforementioned process, a matrix phase kinetic simulation can be developed. Fig. 12(a) presents the thermal histories of surface elements recorded under the four different laser powers during the EHLA process. With a laser spot diameter of 1.4 mm and an offset of 0.2 mm per revolution, each point on the surface experiences direct laser exposure at least seven times (labeled ①–⑦ in the figure). Because the powder is first heated by the laser above its melting point and is subsequently cooled upon contact with the substrate to form the coating, the initiation of cladding occurs at the first track where the substrate surface temperature exceeds the powder liquidus temperature—identified as track ①, which is marked as the cladding start in Fig. 12(a). Owing to the non-negligible thickness increment contributed by each deposited track, the effect of laser energy on the coating temperature diminishes as the layer thickness accumulates, leading to a decrease in the peak temperature from the track ③ onward.

Using the temperature–time profiles in Fig. 12(a) as input, the corresponding effective austenite transformation fractions are shown in Fig. 12(b). Based on the solidification sequence confirmed in Fig. 11—where δ-ferrite solidifies first—the austenite fraction was calculated as a phase transformed from δ-ferrite. Dislocations, grain boundaries, and subgrain boundaries were employed as heterogeneous nucleation sites to model the rapid solidification process. It should be emphasized that this austenite fraction reflects only the transient δ → γ transformation within each track, rather than the actual retained austenite content. Upon cooling to the Ms. temperature, austenite transforms into martensite, meaning that the true austenite fraction at room temperature is zero. The previous EBSD results further confirmed that martensite is the dominant phase, with no retained austenite observed, indicating that the cooling rate was sufficiently high to ensure

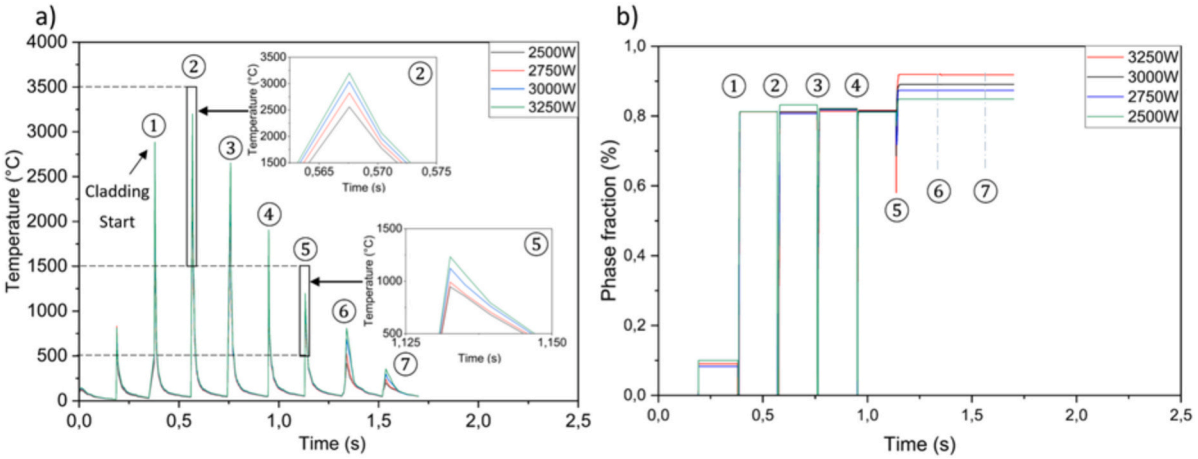

Fig. 12. (a) Thermal history of coating at substrate surface in degree Celsius- second and, (b) kinetics of austenite formation with temperature-time relation from (a). Track ②, which exhibits the highest peak temperature, and track ⑤, where the peak temperature first drops below the liquidus temperature, are shown in enlarged views in (a), respectively,

the complete transformation of austenite into martensite. Meanwhile, in the simulation the austenite fraction is reset to zero whenever the local temperature exceeds the liquidus, which correctly reflects the physical condition that no solid-state phase transformation can occur in the fully molten state during EHLA.

A clear trend is observed: higher laser power produces a higher final effective austenite fraction. The 3250 W condition exhibits the highest value, reaching 91.4%. The primary difference in the fraction stems from the contribution of the final track within the austenitizing temperature range, whereas the intermediate tracks show no direct monotonic dependence on laser power. The transformed austenite content is the lowest at laser power of 2500 W, reaching 84.8%. This trend aligns with the microstructural characteristics observed in the coating No.1 (2500 W PFD = 0 mm) and No.4 (3250 W PFD = 0 mm) described in Section 3.2. This indicates that as laser power increases, the rise in coating hardness stems from an increase in austenite content that is eventually quenched into a larger fraction of martensite.

To further investigate the evolution of phase constituents during

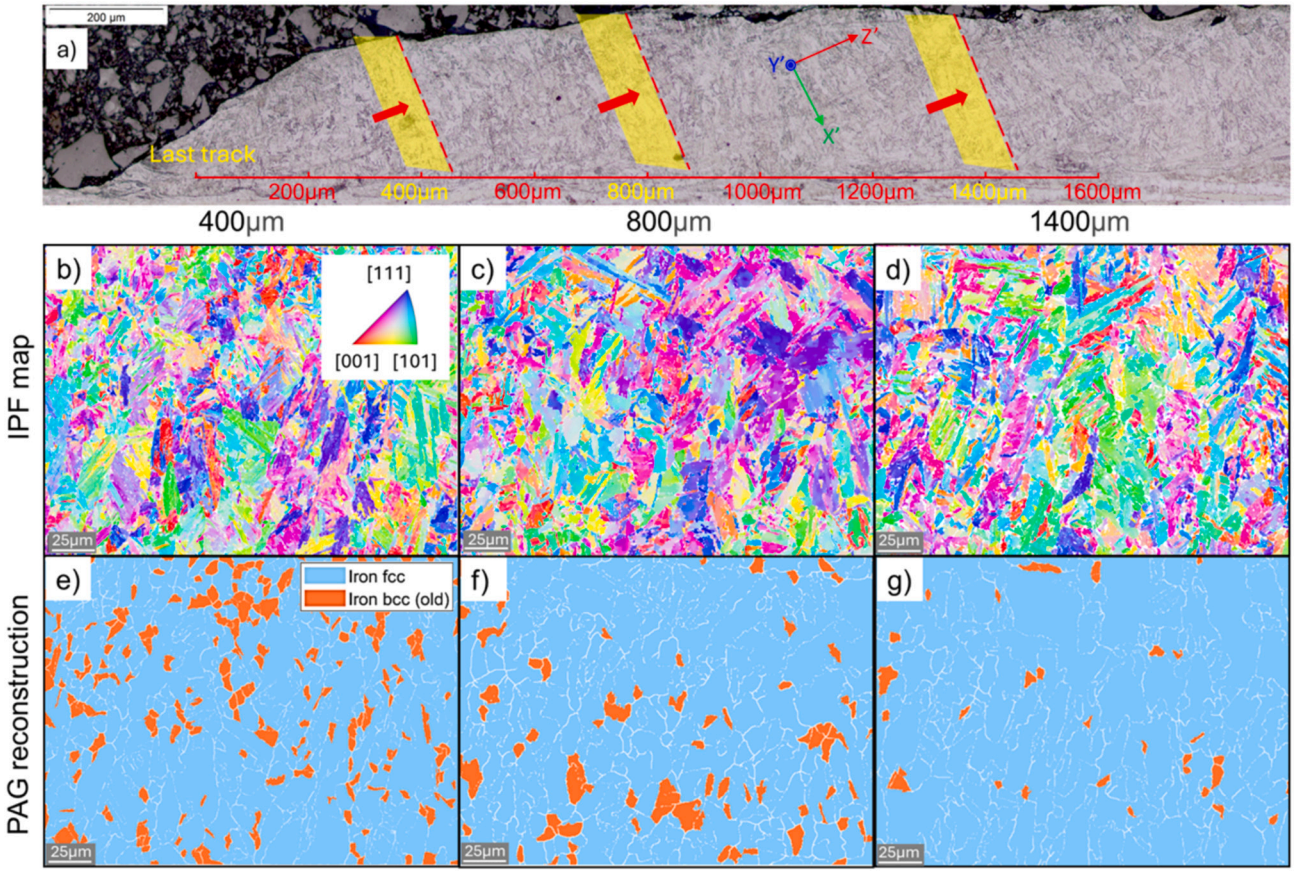

Fig. 13. (a) 3 EBSD Mapping positions in coating geometry of No.4 (3250 W PFD0mm), (b)-(d) IPFD maps and (e)-(g) maps of reconstructed austenite phase(blue) and retained ferrite phase (orange). (For interpretation of the references to colour in this figure legend, the reader is referred to the web version of this article.)

laser processing, the quasi–in-situ approach described in Section 3.2 was adopted. Based on this method, Sample No. 4 (3250 W PFD = 0 mm), which exhibited the highest average hardness, was selected to analyze the phase evolution associated with each individual track.

The preparation of the plane used to examine phase transformations is illustrated in Fig. 13(a). Because the final track does not reach the full average coating thickness, the analysis begins from the second-to-last track, located at 400 μm. The position at 800 μm corresponds to the center of the laser spot of the final track and represents the mid-stage of phase transformation during laser processing. The position at 1400 μm marks the endpoint of the final track; beyond this point, previously deposited tracks were already outside the laser spot and therefore no longer subjected to direct laser heating. In other words, the cumulative phase transformations cease after this location.

The sample was cut and polished at an inclination angle of 60° between longitudinal direction of substrate, enabling a cross-section nearly normal to the fusion line direction and thus capturing grain morphologies as close as possible to the true solidification orientation.

The EBSD results indicate that the coating consists entirely of a BCC phase. Given that 17-4PH exhibits primary solidification as δ-ferrite at high temperature (Fig. 11(a)), and in conjunction with the aforementioned phase kinetics simulation results, the final BCC phase should comprise α-martensite and a small amount of ferrite, as both of these phases are identified as BCC phases in the EBSD results. Since α'-martensite is obtained through the rapid cooling phase transformation of austenite, a microstructural analysis of the parent austenite was conducted to investigate the microstructural evolution under EHLA thermal cycling. A commonly used method for distinguishing martensite and ferrite in EBSD analysis is based on the quality of the EBSD patterns (EBSPs). Ferrite generally tends to produce higher-quality patterns than martensite; therefore, parameters such as image quality (IQ), band contrast (BC), and band slope (BS) are often used for phase distinguishment [47,48]. However, the reliability of this approach strongly depends on the quality of surface preparation. In additively manufactured (AM) materials, the high cooling rates may introduce substantial local strain. Furthermore, distinguishment based solely on pattern quality becomes less reliable when martensite is the dominant phase and both phases exhibit small grain sizes. Therefore, parent austenite reconstruction was employed in the present work to obtain a conservative estimate of the martensite fraction [49]. During reconstruction, neighboring martensitic grains were assigned to the same cluster when their misorientation satisfied the threshold criterion associated with a predefined orientation relationship. Each cluster was then regarded as one reconstructed parent austenite grain and exported for further analysis. In this work, grain misorientation threshold of 5° was applied to distinguish all grain structure of all EBSD results. Austenite reconstruction was performed using the Kurdjumov–Sachs (K—S) crystallographic relationship [50], with the misorientation threshold and tolerance both set to 3.25°. Details of PAG reconstruction and K—S orientation relations together with factors of error function are placed in Appendix 1 and 2.

Fig. 13(b)–(d) show the EBSD–IPF maps obtained at the three selected locations from Fig. 13(a), while Fig. 13(e)–(g) present the corresponding reconstructed austenite phase maps. In these maps, blue denotes grains successfully reconstructed as prior austenite, whereas orange marks grains that could not be reconstructed and were therefore retained ferrite. The fraction of reconstructed austenite, as well as the long-axis and short-axis grain sizes of the reconstructed parent austenite grains, are summarized in the Table 5. The distinction between long and short axes is employed to better reflect the anisotropic grain morphology typical of additively manufactured materials and to analyze the corresponding microstructural evolution. The reconstructed austenite fractions at 400 μm and 800 μm are nearly identical, whereas the reconstruction fraction at 1400 μm is noticeably higher. This result is consistent with the predictions of the kinetic model. In terms of grain size, both the long-axis and short-axis dimensions increase progressively with position. This is consistent with the grain growth characteristics observed under thermal accumulation conditions.

Table 5
Mean long-axis grain size, mean short-axis grain size and reconstructed phase fraction of three positions from EBSD data.

Map position	400 μm	800 μm	1400 μm
Mean long-axis grain size (μm)	24.78	32.07	36.53
Mean short-axis grain size (μm)	11.59	15.43	16.70
Reconstructed phase fraction	79.0%	83.6%	93.1%

3.5. Dilution behavior influenced by laser power and powder focus

To further elucidate the bonding characteristics between the coating and the substrate, as well as the influence of chemical composition, EDS mapping was performed both at the coating–substrate interface and within the coating interior, followed by fine line scans based on the elemental distribution. Because the substrate contains no Cr and the coating possesses a significantly higher Cr content than the other alloying elements, the Cr distribution was used as an indicator to assess how dilution is affected by the laser power and powder focus. Sample No.1 (2500 W PFD = 0 mm), No.4 (3250 W PFD = 0 mm) and No.12 (3250 W PFD = 0.75 mm) were presented as a representative case.

For each sample, four arbitrary line-scan positions were selected across the coating–substrate interface, as indicated by the red lines in **Fig. 14(a), (c)** and **(e)**. The corresponding Cr concentration profiles are shown in **Fig. 14(b), (d)** and **(f)**. **Fig. 14(g)** redraws the horizontal axis from **Fig. 14(f)** to align with the scanning range of the preceding figures. Several engineering guidelines and corrosion studies indicate that chromium levels of ≈11.5–12.5 wt% are required to ensure adequate corrosion resistance in more aggressive environments, particularly in the absence of Mo or Al [51,52]. In line with these findings, a Cr content of 12 wt% was considered the minimum threshold required for corrosion resistance [53]. The maximum distance over which the Cr content falls below this threshold is highlighted by a black box, and the location where the Cr content first returns to the same level along the same scan is used to define the maximum dilution distance. These distances are marked on each Cr-distribution plot. A larger maximum dilution distance indicates that the Cr-depleted region extends closer to the coating surface, implying an earlier onset of corrosion-related failure.

At a powder focus of 0 mm, the maximum dilution distances of the coatings are very similar; however, the Cr concentration at the maximum dilution distance increases with increasing laser power. At higher distances from the interface, the Cr concentration inside the coating gradually reaches a steady level, and this steady-state Cr content decreases as the laser power increases. It is noteworthy that in Sample No. 12 (3250 W PFD = 0.75 mm) in **Fig. 14(e)**, a pronounced diluted region remains in the upper portion of the coating far from the interface, necessitating an extended EDS scanning range. Such long-range dilution was not observed in the other samples.

Near the coating–substrate interface, the homogeneity of the Cr distribution improves with increasing powder focus, and the regions with Cr contents below 12 wt% become smaller. This indicates that increasing PFD promotes a more chemically uniform interface between the coating and the substrate. As the powder focus increases from 0 to 0.75 mm, the overall Cr content in the middle of the coating increases slightly, suggesting that at PFD = 0 mm, repeated thermal cycles cause previously diluted regions to undergo further mixing with the substrate. This trend is reflected in the maximum dilution distance (highlighted by the black boxed regions in the figure), which decreases as the PFD increases.

To more accurately characterize the behavior at the interface of coating–substrate dilution, high-resolution EDS line scans of Cr were performed at the coating–substrate interface for six representative samples shown in Fig. 15, using a step size of 0.2 μm. The scanning width

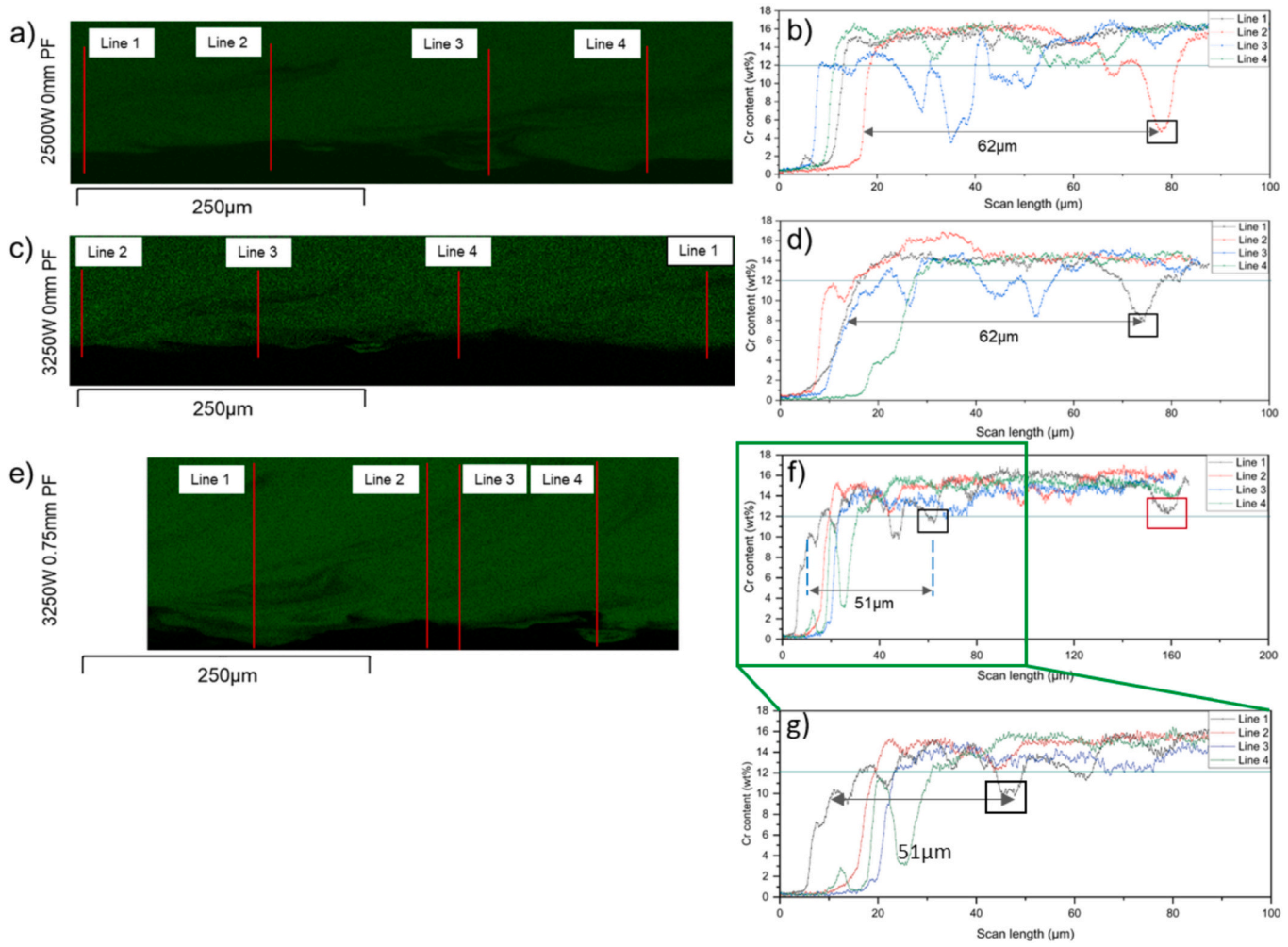

Fig. 14. (a), (c) and (e) EDS map results with line scan positions and (b), (d) and (f) line scan diagrams, (g) zoomed in on line scan in (f) to 100 μm. (f) highlights the chromium-depleted zone within the coating (red) far from the coating-substrate interface.

is 40 μm, ensuring sufficient line length to capture the elemental distribution at the coating-substrate interface. Owing to inhomogeneous melt mixing in the fusion zone, the Cr concentration profile does not consistently follow the one-dimensional error-function-type distribution [54]. The regions that conform to liquid-state diffusion behavior are highlighted in the figure. In most cases, the Cr concentration initially exhibits a diffusion-controlled gradient from the substrate toward the coating, followed by a transition into an unstable mixing region. Beyond this region, the Cr gradient often decreases, and in certain locations the Cr content drops due to excessive entrainment of substrate material into the melt pool.

Notably, in sample No.1 (2500 W PFD = 0 mm) and No.2 (2750 W PFD = 0 mm), two separated diffusion-like regions exceeding 20 μm were observed along line scan 3. In the No.12 coating (3250 W PFD = 0.5 mm), a Cr-depleted zone appears at approximately 25 μm along line scan 4. These observations collectively indicate that the interaction between the molten powder and the substrate is inherently inhomogeneous during deposition. Moreover, the extremely high cooling rate in EHLA shortens the lifetime of the liquid phase, limiting solute diffusion; as a result, Cr-depleted regions formed during unstable mixing are retained within the solidified coating.

The diffusion-controlled dilution zones at the coating–substrate interface for all samples are highlighted in Fig. 15. A clear trend is observed in Fig. 15(a)–(d): as the laser energy input increases, the Cr concentration gradient at the interface becomes progressively less steep. This behavior arises because higher laser energy prolongs the time during which the coating and substrate remain in the liquid state, thereby enhancing solute diffusion and leading to a more gradual concentration transition across the interface.

The influence of powder focus on the interfacial Cr gradient can be assessed from Fig. 15(d)–(f). With increasing powder focus, the Cr concentration gradient becomes noticeably steeper. Analogous to the effect of laser power, increasing the powder focus effectively reduces the extent of liquid-state mixing between the coating and the substrate, thereby preserving a sharper compositional transition at the interface.

Based on the EDS mapping results above; two distinct forms of dilution can be identified within the EHLA-produced coatings. The first is diffusion-dominated dilution occurring at the coating–substrate interface, which provides the basis for stable metallurgical bonding. The second is non-diffusional dilution i.e., convective dilution, appearing at locations far from the interface, as clearly evidenced by the Cr distribution maps. From a physical–mechanistic standpoint, the first type can be reasonably approximated by a one-dimensional diffusion model acting across a planar interface between the coating and the substrate. In contrast, the second type originates from mechanical entrainment of substrate melt convection mixing into the molten coating, followed by incomplete solute exchange under rapid solidification. These convection regions subsequently solidify as locally Cr-depleted zones and remained within the coating. The following sections discuss these two dilution mechanisms separately.

In the case of single-layer coatings where dilution at the interface is dominated by diffusion, most previous studies have focused on

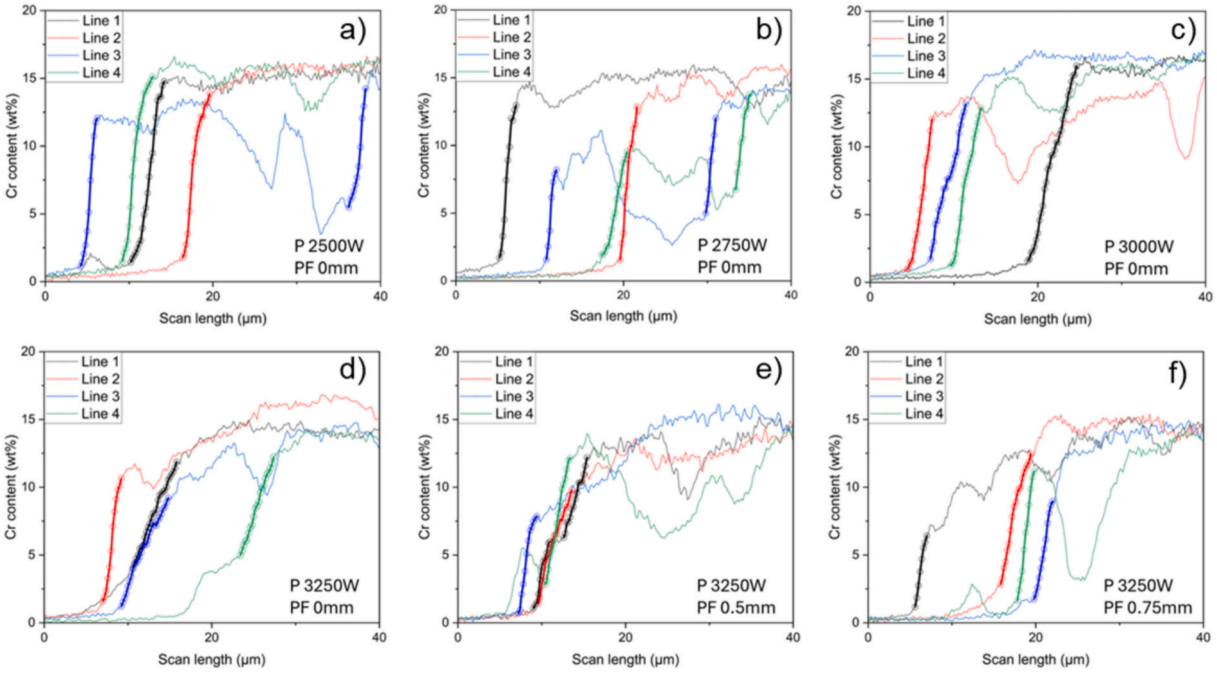

Fig. 15. EDS diagrams on line scanning at the coating–substrate interface acquired with a 0.2 μm step size of 6 coatings. Bonds with typical diffusive behavior at the coating – substrate interfaces are highlighted.

geometric dilution, estimating the dilution ratio based on melt pool depth and coating thickness [55,56]. It is well established that the dilution ratio generally increases with higher line energy density (i.e., higher laser power or lower scan speed) and decreases with higher powder mass flow rate or faster scanning speed [57–59]. These parameters fundamentally govern the extent of substrate melting under the influence of process energy, thereby controlling the degree of intermixing between base metal and powder, and ultimately determining diffusion depth and dilution behavior.

Unlike diffusion-dominated dilution, dilution occurring at a certain distance from the coating–substrate interface does not originate from atomic diffusion within the material. Instead, it is caused by convective mixing between the melt generated by substrate melting and the molten additive material. This non-diffusive mechanism is referred to herein as

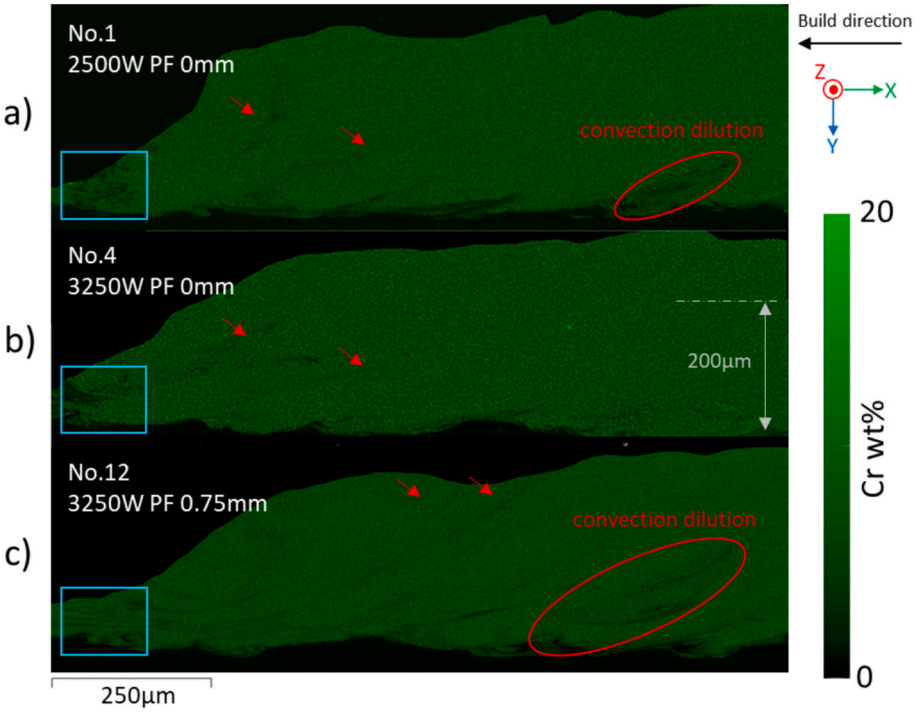

Fig. 16. Cr distribution at last tracks of sample No.1(2500 W, PFD 0 mm) No.4(3250 W, PFD 0 mm) and No.12(3250 W, PFD 0.75 mm). Convection-induced dilutions are highlighted in red and convection mixing are shown in blue box respectively. Red arrows show the evidence of typical convection-induced dilutions. (For interpretation of the references to colour in this figure legend, the reader is referred to the web version of this article.)

convection-induced dilution. The resulting dilution front typically exhibits a curved morphology with a finite volume. Previous studies on such convection phenomena have mainly focused on experimental observation and numerical simulation of capillary flow and Marangoni convection at the leading edge of the melt pool under laser irradiation [60–63]. In the present work, convection-induced dilution within the coating is analyzed through Cr distributions in the final deposited tracks, as illustrated in Fig. 16.

For all three laser parameter sets, pronounced coating–substrate convection was observed in the final track, as highlighted by the blue boxes in Fig. 16. In addition, chromium-depleted regions induced by this convective behavior were identified in the adjacent tracks (marked by red arrows). For sample No. 12 (3250 W, PFD = 0.75 mm), convection dilution extended to the surface of the coating, which is consistent with the chromium-depleted zone observed near the coating surface in **Fig. 14(f)**. In contrast, for sample No. 1 (2500 W, PFD = 0 mm), the convective dilution was confined to the middle of the track, with no evident dilution near the surface. Although the highest laser power was carried out in sample No. 4 (3250 W, PFD = 0 mm), no pronounced convection-induced dilution was observed within the coating except for the final track.

To further clarify the effect of laser power on convection-induced dilution at an identical powder focus distance, as well as the distinct dilution behavior observed at two powder focus distances under a laser power of 3250 W, the average chemical composition was measured with EDS at a location 200 μm above the coating–substrate interface. The results are summarized in Table 6. For sample No. 1 (2500 W, PFD = 0 mm), the chromium content near the surface is nearly identical to that of the powder feedstock, indicating that convection-induced dilution is restricted to a narrow region close to the interface and does not significantly influence the entire coating. In contrast, the chromium contents of the two coatings fabricated at 3250 W with different powder focus distances (0 mm and 0.75 mm) are comparable, both are substantially lower than the chromium content of the powder. Notably, for sample No. 4 (3250 W, PFD = 0 mm), despite the absence of an apparent convection-induced dilution zone at 200 μm from the interface, the chromium content remains lower than that of sample No. 12 (3250 W, PFD = 0.75 mm).

These results suggest that: (i) increasing the powder focus distance effectively reduces the thermal influence on previously deposited tracks, such that internal dilution zones cannot be fully homogenized by intrinsic heat effects; (ii) although sample No. 4 (3250 W, PFD = 0 mm) does not exhibit pronounced local chromium depletion by dilution, the apparent uniform chromium distribution is achieved through compositional averaging, resulting in an overall reduction in chromium content across the coating; and (iii) reducing the laser energy input is an effective strategy for mitigating the global impact of convection-induced dilution on coating composition.

The influence of laser power on convective dilution can be interpreted using the schematic shown in Fig. 17. At a laser power of 2500 W, the relatively low heat input results in a limited amount of substrate material being melted and involved in convective transport. Moreover, according to the simulation result of temperature–time history in Fig. 10 (a), the lower laser power significantly shortens the liquid phase duration, further restricting the transportation of convective flow into the coating. The combination of these two effects causes convective dilution to be confined to the vicinity of the coating–substrate interface, as illustrated in Fig. 17(a). By contrast, increasing the laser power results in a greater amount of substrate material melting and participating in convective mixing with the coating material, accompanied by a prolonged lifetime of the convective flow. This significantly intensifies convective dilution of Cr- free substrate into coating materials, which is consequently reflected by an overall decrease in the chromium content throughout the coating.

Table 6
Chemical composition of alloy elements at 200 μm above the coating–substrate interface.

Chemical composition	Cr	Ni	Cu	Nb
No.1 2500 W PFD 0 mm	16.88	4.46	3.90	0.26
No.4 3250 W PFD 0 mm	15.14	4.16	3.41	0.22
No.12 3250 W PFD 0.75 mm	15.92	4.27	3.44	0.23

4. Conclusions

The present study demonstrates that dense 17-4PH coatings with a nearly fully martensitic structure and good metallurgical bonding to the substrate can be produced by the EHLA process when using a laser power of 3250 W in combination with powder focus distances (PFDs) of 0, 0.5, and 0.75 mm. These results provide a feasible basis for achieving the goal of ‘as-built is finish’ and offer a new perspective for process parameter optimization and alloy design in EHLA-fabricated coatings. Based on the analysis of EHLA-fabricated 17-4PH coatings produced under different processing conditions, the following conclusions can be drawn:

- At a constant laser power, different powder focus distances (PFD) had little influence on the coating thickness or the mean dilution depth. The laser power was identified as the dominant factor affecting the dilution depth. However, increasing the PFD improved the stability of dilution depth.
- At a constant powder focus, increasing the laser power led to a higher martensite fraction in the final track due to the cumulative phase transformation occurring within the austenitic temperature range, which in turn resulted in increased hardness. This trend was consistently confirmed by both phase transformation simulations and experimental results.
- Diffusion-controlled dilution occurs at the coating–substrate interface, establishing a stable metallurgical bond. The concentration gradient decreases and the diffusion layer thickness increase with increasing laser power, whereas increasing powder focus yields the opposite trend—steeper concentration gradients and a thinner diffusion thickness.
- Convection-induced dilution appears within the interior of the coating, posing challenges for the corrosion resistance of 17-4PH stainless-steel coatings. Higher laser power and lower powder focus distance help suppress this type of dilution behavior by resulting in a reduction in the overall Cr content but promoting a more homogeneous Cr distribution within the coating.

Finally, the selection of laser power and powder focus distance (PFD) should be taken into consideration of the specific characteristics of the coating material. In the present study, a relatively high laser power was employed to obtain a fully martensitic 17-4PH coating. However, this also resulted in an increased dilution ratio and subsequently a greater chromium depletion. For non-martensitic Fe-based coatings, by contrast, process optimization should give priority to an increased PFD combined with a lower laser power, particularly when coating quality is evaluated in terms of coating morphology and dilution behavior.

CRediT authorship contribution statement

Bohang Gao: Writing – original draft, Visualization, Software, Methodology, Investigation, Formal analysis, Data curation, Conceptualization. **Stefanie Linnenbrink:** Writing – review & editing, Visualization, Resources, Methodology, Investigation, Data curation, Conceptualization. **Norbert Pirch:** Visualization, Software, Methodology, Data curation, Conceptualization. **Ulrich Krupp:** Writing – review & editing, Validation, Supervision, Project administration, Funding

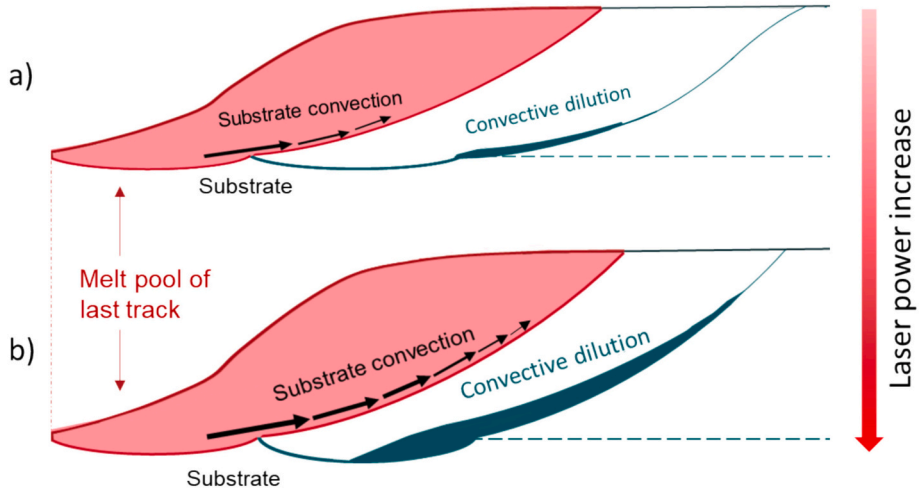

Fig. 17. Schematic diagram showing the influence of laser power on convection-induced dilution.

acquisition, Conceptualization.

Declaration of competing interest

The authors declare that they have no known competing financial interests or personal relationships that could have appeared to influence the work reported in this paper.

Acknowledgements

The authors acknowledge funding received by the Industrielle Gemeinschaftsforschung and Forschungsvereinigung Stahlanwendung (IGF-FOSTA) project 01IF22549N in program 'Development of in-situ hardening Fe-based alloy for corrosion and wear protection using laser cladding'. The authors gratefully acknowledge Felix Oppermann from IEHK (Steel Institute), RWTH Aachen University, for his assistance with English language editing and proofreading of the manuscript.

Appendix A

Based on the specific orientation relationships associated with the austenite-to-martensite transformation, the parent (prior) austenite phase can be reconstructed. This serves two purposes: firstly, to investigate the grain growth behavior of the parent austenite under thermal cycle; and secondly, to investigate the evolution of the reconstructed phase fraction over the course of thermal cycling. The reconstruction takes into account 24 K-S orientation relationships, which serve as the basis for reconstructing the original austenite, as shown in Fig. 1.

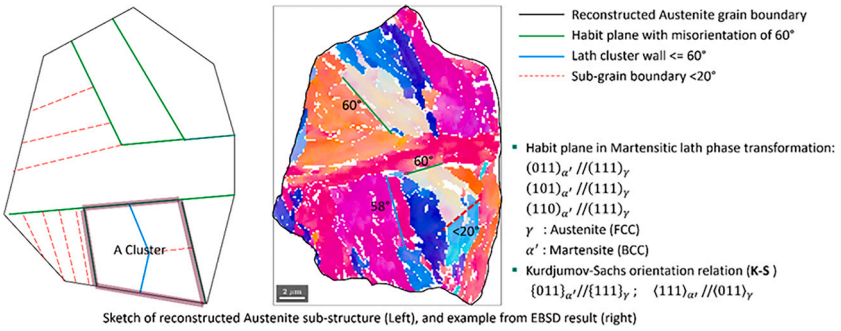

Appendix Fig. 1. K—S orientation relation and a PAG example. The specific misorientations are highlighted and.

During variant identification and PAG reconstruction, a 3.25° threshold and 3.25° tolerance were used to account for misorientations between martensitic grains (child to child grains, C2C) and to reconstruct the austenitic matrix with clusters made of C2C pairs. 3.25 degree is the fitted value for the left asymptote; to facilitate comparison, the fitted value of 3.75 for the right asymptote has also been included in the Fig. 2.

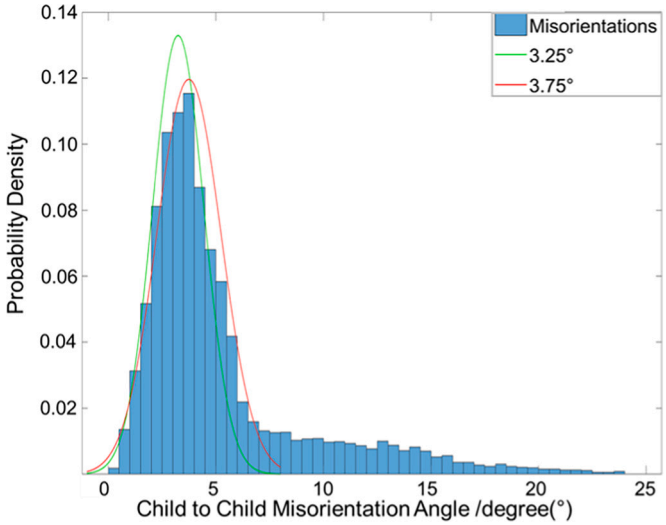

Appendix Fig. 2. Error function used for threshold and tolerance value 3.25 degree (left asymptote) shown in green and 3.75 degree (right asymptote) in red.

Data availability

Data will be made available on request.

References

[1] L. Quintino, Overview of coating technologies, in: Surface Modification by Solid State Processing, Woodhead Publishing, 2014, pp. 1–24.
[2] T. Schopphoven, A. Gasser, G. Backes, EHLA: extreme high-speed laser material deposition: economical and effective protection against corrosion and wear, Laser Technik Journal 14 (4) (2017) 26–29.
[3] Y. Liang, Z.Y. Liao, L.L. Zhang, M.W. Cai, X.S. Wei, J. Shen, A review on coatings deposited by extreme high-speed laser cladding: processes, materials, and properties, Opt. Laser Technol. 164 (2023) 109472.
[4] T. Schopphoven, A. Gasser, K. Wissenbach, R. Poprawe, Investigations on ultra-high-speed laser material deposition as alternative for hard chrome plating and thermal spraying, J. Laser Appl. 28 (2) (2016).
[5] Y. Ren, L. Li, Y. Zhou, S. Wang, In situ synthesized VC reinforced Fe-based coating by using extreme high-speed laser cladding, Mater. Lett. 315 (2022) 131962.
[6] M.U. Ko, J. Cüppers, T. Schopphoven, C. Häfner, Extreme high-speed DED of AISI M2 steel for coating application and additive manufacturing, Coatings 14 (8) (2024) 953.
[7] K. Qi, Y. Yang, Microstructure, wear, and corrosion resistance of Nb-modified magnetic field-assisted co-based laser cladding layers, Surf. Coat. Technol. 434 (2022) 128195.
[8] Y. Xu, G. Wang, Q. Song, X. Lu, Z. Li, Q. Zhao, Y. Chen, Microstructure, mechanical properties, and corrosion resistance of SiC reinforced AlxCoCrFeNiTi1-x high-entropy alloy coatings prepared by laser cladding, Surf. Coat. Technol. 437 (2022) 128349.
[9] Y. Wu, J. Barras, J. Gutjahr, C. Hauser, Y.T. Tang, R.C. Reed, W.M. Rainforth, Extreme high-speed laser application of coating to prevent hydrogen embrittlement in metals, in: AMPP Corrosion (pp. AMPP-2023), AMPP, 2023, March.
[10] S. Koß, S. Vogt, M. Göbel, J.H. Schleifenbaum, Coating of aluminum with high deposition rates through extreme high-speed laser application, J. Therm. Spray Technol. 32 (6) (2023) 1689–1697.
[11] Y. Liang, Z.Y. Liao, L.L. Zhang, M.W. Cai, X.S. Wei, J. Shen, A review on coatings deposited by extreme high-speed laser cladding: processes, materials, and properties, Opt. Laser Technol. 164 (2023) 109472.
[12] N. Haghdadi, M. Laleh, M. Moyle, S. Primig, Additive manufacturing of steels: a review of achievements and challenges, J. Mater. Sci. 56 (1) (2021) 64–107.
[13] C. Zitelli, P. Folgarait, A. Di Schino, Laser powder bed fusion of stainless-steel grades: a review, Metals 9 (7) (2019) 731.
[14] M.H. Nie, S. Zhang, Z.Y. Wang, T.Y. Yin, C.H. Zhang, C.L. Wu, D.X. Zhang, Laser cladding of 17-4 PH stainless steel coatings: microstructure, texture characterization, and corrosion resistance, J. Mater. Eng. Perform. 32 (12) (2023) 5545–5553.
[15] D. Guo, J. Chen, X. Chen, Q. Shi, V.A.M. Cristino, C.T. Kwok, X. Li, Pitting corrosion behavior of friction-surfaced 17-4PH stainless steel coatings with and without subsequent heat treatment, Corros. Sci. 193 (2021) 109887.
[16] M. Alnajjar, F. Christien, K. Wolski, C. Bosch, Evidence of austenite by-passing in a stainless steel obtained from laser melting additive manufacturing, Addit. Manuf. 25 (2019) 187–195.
[17] C.Y. Yap, C.K. Chua, Z.L. Dong, Z.H. Liu, D.Q. Zhang, L.E. Loh, S.L. Sing, Review of selective laser melting: materials and applications, Appl. Phys. Rev. 2 (4) (2015).
[18] M.P. Haines, M.S. Moyle, V.V. Rielli, N. Haghdadi, S. Primig, Site-specific cu clustering and precipitation in laser powder-bed fusion 17–4 PH stainless steel, Scr. Mater. 241 (2024) 115891.
[19] Y.H. Cho, S.Y. Park, J.Y. Kim, K.A. Lee, 17-4PH stainless steel with excellent strength–elongation combination developed via material extrusion additive manufacturing, J. Mater. Res. Technol. 24 (2023) 3284–3299.
[20] A. Ozsoy, E. Aydogan, A.F. Dericioglu, Selective laser melting of Nano-TiN reinforced 17-4 PH stainless steel: densification, microstructure and mechanical properties, Mater. Sci. Eng. A 836 (2022) 142574.
[21] S. Vunnam, A. Saboo, C. Sudbrack, T.L. Starr, Effect of powder chemical composition on the as-built microstructure of 17-4 PH stainless steel processed by selective laser melting, Addit. Manuf. 30 (2019) 100876.
[22] S.D. Meredith, J.S. Zuback, J.S. Keist, T.A. Palmer, Impact of composition on the heat treatment response of additively manufactured 17–4 PH grade stainless steel, Mater. Sci. Eng. A 738 (2018) 44–56.
[23] L.E. Murr, E. Martinez, J. Hernandez, S. Collins, K.N. Amato, S.M. Gaytan, P. W. Shindo, Microstructures and properties of 17-4 PH stainless steel fabricated by selective laser melting, J. Mater. Res. Technol. 1 (3) (2012) 167–177.
[24] M.S. Moyle, N. Haghdadi, F. Theska, M.P. Haines, X.Z. Liao, S.P. Ringer, S. Primig, Effect of compositional variations on the heat treatment response in 17-4 PH stainless steel fabricated by laser powder bed fusion, Mater. Charact. 209 (2024) 113768.
[25] M. Schmidt, H. Naesstroem, J. Volpp, K. Partes, Relating melt mixing, dilution and vapor emissions during directed energy deposition, Opt. Laser Technol. 181 (2025) 111824.
[26] D.T. Sarathchandra, M.J. Davidson, G. Visvanathan, Parameters effect on SS304 beads deposited by wire arc additive manufacturing, Mater. Manuf. Process. 35 (7) (2020) 852–858.
[27] K. Zhang, X.M. Zhang, W.J. Liu, Influences of processing parameters on dilution ratio of laser cladding layer during laser metal deposition shaping, Adv. Mater. Res. 549 (2012) 785–789.
[28] S. Zhu, W. Xia, H. Kamali, L. Ouyang, L. Xie, Z. Huang, Z. Jiang, Deep learning-driven precision control of dilution rate in multi-pass laser cladding: experiment and simulation, Int. J. Adv. Manuf. Technol. 127 (11) (2023) 5353–5371.
[29] C. Böhm, M. Werz, S. Weihe, Dilution ratio and the resulting composition profile in dissimilar laser powder bed fusion of AlSi10Mg and Al99. 8, Metals 10 (9) (2020) 1222.
[30] T. Li, L. Zhang, G.G.P. Bultel, T. Schopphoven, A. Gasser, J.H. Schleifenbaum, R. Poprawe, Extreme high-speed laser material deposition (EHLA) of AISI 4340 steel, Coatings 9 (12) (2019) 778.
[31] Z. Chen, Z. Guo, Y. Zeng, Z. Li, Y. Wang, G. Wang, Y. Hu, Study on microstructure and properties of AlCoCrFeNi high-entropy alloys by extreme high-speed laser cladding, Coatings 14 (11) (2024) 1394.
[32] O. Abdulhameed, A. Al-Ahmari, W. Ameen, S.H. Mian, Additive manufacturing: challenges, trends, and applications, Adv. Mech. Eng. 11 (2) (2019) 1687814018822880.
[33] M.T. Getachew, M.Z. Shiferaw, B.S. Ayele, Recent advances of additive manufacturing for aerospace industries: methods, materials, challenges, and future outlooks, Sustainable Development Research in Manufacturing, Process Engineering, Green Infrastructure, and Water Resources: Advancement of Science and Technology (2025) 47–82.

[34] R. Han, H. Zhang, J. Liu, S. Li, L. Xu, M. Zhang, H. Chen, Investigation on the fatigue behavior of different extreme high-speed laser cladding materials on the damaged EA4T axle, J. Mater. Res. Technol. 37 (2025) 629–645.
[35] F. Bachmann, R. Hielscher, H. Schaeben, Texture analysis with MTEX–free and open-source software toolbox, Solid State Phenom. 160 (2010) 63–68.
[36] N. Pirch, Influence of powder-laser interaction on heat flux distribution, laser material deposition, Presented at ICALEO 2025, Orlando, FL, Oct. 2025.
[37] J.O. Andersson, T. Helander, L. Höglund, P. Shi, B. Sundman, Thermo-Calc & DICTRA, computational tools for materials science, Calphad 26 (2) (2002) 273–312.
[38] E. Kozeschnik, B. Buchmayr, MATCALC-a simulation tool for multicomponent thermodynamics, diffusion and phase transformations, in: Mathematical Modelling of Weld Phenomena: vol. No. 5, CRC Press, 2024, pp. 349–361.
[39] J. Svoboda, F.D. Fischer, P. Fratzl, E. Kozeschnik, Modelling of kinetics in multi-component multi-phase systems with spherical precipitates: I: theory, Mater. Sci. Eng. A 385 (1–2) (2004) 166–174.
[40] U. De Oliveira, V. Ocelík, J.T.M. De Hosson, Analysis of coaxial laser cladding processing conditions, Surf. Coat. Technol. 197 (2–3) (2005) 127–136.
[41] Y. Jian, Y. Liu, H. Qi, P. He, G. Huang, Z. Huang, Effects of scanning speed on the microstructure, hardness and corrosion properties of high-speed laser cladding Fe-based stainless coatings, J. Mater. Res. Technol. 29 (2024) 3380–3392.
[42] Y. Xu, B. Mishra, S.P. Narra, Experimental investigation of in-situ microstructural transformations in wire arc additively manufactured maraging 250-grade steel, Mater. Charact. 190 (2022) 112065.
[43] A. Marques, A. Cunha, M.R. Silva, M.I. Osendi, F.S. Silva, O. Carvalho, F. Bartolomeu, Inconel 718 produced by laser powder bed fusion: an overview of the influence of processing parameters on microstructural and mechanical properties, Int. J. Adv. Manuf. Technol. 121 (9) (2022) 5651–5675.
[44] F. Lambiase, P.B. Yanala, A. Paoletti, Thermal, microstructural, and mechanical characterization of early-stage deposition in wire arc additive manufacturing, Int. J. Adv. Manuf. Technol. (2025) 1–18.
[45] D. Svetlizky, B. Zheng, D.M. Steinberg, J.M. Schoenung, E.J. Lavernia, N. Eliaz, The influence of laser directed energy deposition (DED) processing parameters for Al5083 studied by central composite design, J. Mater. Res. Technol. 17 (2022) 3157–3171.
[46] S.H. Lee, J.H. Koo, O. Cakmak, J.W. Cho, Effect of laser power during laser powder bed fusion on microstructure of joining interface between tungsten and AISI 316L steel, Additive Manufacturing Letters 11 (2024) 100246.
[47] A.A. Gazder, F. Al-Harbi, H.T. Spanke, D.R. Mitchell, E.V. Pereloma, A correlative approach to segmenting phases and ferrite morphologies in transformation-induced plasticity steel using electron back-scattering diffraction and energy dispersive X-ray spectroscopy, Ultramicroscopy 147 (2014) 114–132.
[48] J.Y. Kang, Qualities of electron backscatter diffraction patterns and image contrast from a ferritic-martensitic steel microstructure, Mater. Charact. 187 (2022) 111826.
[49] G. Miyamoto, N. Iwata, N. Takayama, T. Furuhara, Mapping the parent austenite orientation reconstructed from the orientation of martensite by EBSD and its application to ausformed martensite, Acta Mater. 58 (19) (2010) 6393–6403.
[50] F. Niessen, T. Nyyssönen, A.A. Gazder, R. Hielscher, Parent grain reconstruction from partially or fully transformed microstructures in MTEX, Applied Crystallography 55 (1) (2022) 180–194.
[51] P.-J. Cunat, Alloying Elements in Stainless Steel and Other Chromium-Containing Alloys, Euro Inox, 2004.
[52] C. Örnek, M.A. Brennan, U. Izagirre, L.P. Willemse, M.J. Duarte, Understanding the passive behaviour of low-chromium stainless steels, npj Materials Degradation 7 (8) (2023) 1–12.
[53] J.R. Davis (Ed.), Corrosion: Understanding the Basics, ASM International, Materials Park, OH, 2000, p. 38.
[54] O.O. Barah, F. Natukunda, I. Bori, K.J. Ukagwu, Mechanisms and modelling of diffusion in solids: a multiscale framework with industrial case studies and AI enhancements, Discov. Sustain. 6 (1) (2025) 804.
[55] S.S. Chakraborty, S. Dutta, Estimation of dilution in laser cladding based on energy balance approach using regression analysis, Sādhanā 44 (6) (2019) 150.
[56] Y. Li, K. Wang, H. Fu, X. Zhi, X. Guo, J. Lin, Prediction for dilution rate of AlCoCrFeNi coatings by laser cladding based on a BP neural network, Coatings 11 (11) (2021) 1402.
[57] Y. Qiao, J. Huang, D. Huang, J. Chen, W. Liu, Z. Wang, Z. Zhibin, Effects of laser scanning speed on microstructure, microhardness, and corrosion behavior of laser cladding Ni45 coatings, J. Chemother. 2020 (1) (2020) 1438473.
[58] W. Gao, S. Wang, Y.X. Tian, H. Lu, H. Liu, H. Yu, D. Sun, Effect of the powder feeding rate on the microstructure and properties of the laser-cladded titanium coating, J. Mater. Res. Technol. 38 (2025) 4676–4687.
[59] M. Yamaguchi, N. Kato, Y. Funada, T. Yachi, A. Saikai, T. Furumoto, Influence of the laser power and powder feed rate on the porosity, dilution, and building efficiency of pure copper parts fabricated via directed energy deposition with a blue laser, Int. J. Adv. Manuf. Technol. 135 (11) (2024) 5235–5251.
[60] L. Liu, G. Wang, K. Ren, Y. Di, L. Wang, Y. Rong, H. Wang, Marangoni flow patterns of molten pools in multi-pass laser cladding with added nano-CeO2, Addit. Manuf. 59 (2022) 103156.
[61] V. Ocelík, O. Nenadl, A. Palavra, J.T.M. De Hosson, On the geometry of coating layers formed by overlap, Surf. Coat. Technol. 242 (2014) 54–61.
[62] P. Lyu, P. Li, K. Jiang, Numerical simulation and experimental investigation of the laser cladding processes of Ti6Al4V with coaxial shroud protection, J. Mater. Res. Technol. 26 (2023) 4133–4150.
[63] O.B. Kovalev, D.V. Bedenko, A.V. Zaitsev, Development and application of laser cladding modeling technique: from coaxial powder feeding to surface deposition and bead formation, Appl. Math. Model. 57 (2018) 339–359.